

Coherent Control of Quantum-Dot Spins with Cyclic Optical Transitions

Zhe Xian Koong,^{1,*} Urs Haeusler,¹ Jan M. Kaspari,² Christian Schimpf,¹ Benyam Dejen,¹ Ahmed M. Hassanen,^{1,3} Daniel Graham,¹ Ailton J. Garcia Jr.,⁴ Melina Peter,⁴ Edmund Clarke,⁵ Maxime Hugues,⁶ Armando Rastelli,⁴ Doris E. Reiter,² Mete Atatüre,^{1,†} and Dorian A. Gangloff^{1,‡}

¹*Cavendish Laboratory, University of Cambridge, JJ Thomson Ave, Cambridge CB3 0HE, United Kingdom*

²*Department of Physics, TU Dortmund University, 44227 Dortmund, Germany*

³*Department of Engineering Science, University of Oxford, Parks Road, OX1 3PJ, United Kingdom*

⁴*Institute of Semiconductor and Solid State Physics, Johannes Kepler University, Linz, Austria*

⁵*EPSRC National Epitaxy Facility, University of Sheffield, Broad Lane, Sheffield S3 7HQ, United Kingdom*

⁶*Université Côte d'Azur, CNRS, CRHEA, rue Bernard Gregory, 06560 Valbonne, France*

(Dated: September 19, 2025)

Solid-state spins are promising as interfaces from stationary qubits to single photons for quantum communication technologies. Semiconductor quantum dots have excellent optical coherence, exhibit near-unity collection efficiencies when coupled to photonic structures, and possess long-lived spins for quantum memory. However, the incompatibility of performing optical spin control and single-shot readout simultaneously has been a challenge faced by almost all solid-state emitters. To overcome this, we leverage light-hole mixing to realize a highly asymmetric lambda system in a negatively charged heavy-hole exciton in Faraday configuration. By compensating GHz-scale differential Stark shifts, induced by unequal coupling to Raman control fields, and by performing nuclear-spin cooling, we achieve quantum control of an electron-spin qubit with a π -pulse contrast of 97.4% while preserving spin-selective optical transitions with a cyclicity of 409. We demonstrate this scheme for both GaAs and InGaAs quantum dots, and show that it is compatible with the operation of a nuclear quantum memory. Our approach thus enables repeated emission of indistinguishable photons together with qubit control, as required for single-shot readout, photonic cluster-state generation, and quantum repeater technologies.

I. INTRODUCTION

Quantum network nodes based on efficient, long-lived spin-photon interfaces are essential for distributed quantum information processing [1–3]. Each node consists of an interface between single photons and a spin qubit, and realizing its full functionality requires initializing and reading out the spin state, encoding information via quantum control over the spin, entangling the spin with a photon, and storing this quantum information in a local memory before sending the photon across the optical link [4, 5]. These requirements typically reduce to the simultaneous ability to coherently control a long-lived spin ground state, and to trigger spin-selective emission of photons via cyclic transitions. While direct magnetic-dipole control of the ground state spin is possible in several systems with cyclic transitions [6–8], in many quantum emitter systems this remains an outstanding problem to integrate with efficient photonic structures [9], and all-optical means are thus the only viable route for quantum control. However, all-optical control requires linking the spin states via multiple allowed optical transitions can conflict directly with the need for cyclic optical transitions.

Amongst quantum emitters, semiconductor quantum

dots (QDs) stand out for their exceptional optical coherence and efficiency, thanks to the continued improvement in material quality [10, 11] and photonic technologies [12, 13]. They also feature coherent electronic and nuclear spins [14–17], such that 100-microsecond [18] and 100-millisecond [19] coherence times are attainable for GaAs QDs, respectively. While some low-field control of the spin is possible with limited fidelity [20], addressing and controlling the electronic spin as a high-fidelity qubit typically requires a few-Tesla magnetic field to lift the degeneracy of the electronic spin states beyond the scale of hyperfine and exciton linewidth energies. Under a growth-axis field (Faraday configuration), the presence of circularly polarized cyclic transitions allows for efficient spin-selective readout [21, 22] in the single-shot regime [23, 24]. However, spin control of a QD in this configuration has not been realized. Direct microwave drive would need to operate in the few to tens of GHz regime and would need to reach Rabi frequencies of tens of MHz at minimum – for nuclear-spin stabilization of the qubit splitting [25] – corresponding to tens of mT of magnetic flux density at the QD position; this is a formidable challenge for optically active QD systems. The historical and viable approach for spin control in a QD has thus been to apply an in-plane field (Voigt configuration), resulting in a symmetric linearly polarized Λ system which allows all-optical coherent control over the spin states [14, 25–29], reaching high contrast (99.3% [18]) and full-phase control of an electronic spin with GHz-scale Rabi frequency [29]. Despite efforts to selectively enhance a readout transition in this

* Corresponding author: zxk22@cam.ac.uk

† Corresponding author: ma424@cam.ac.uk

‡ Corresponding author: dag50@cam.ac.uk

configuration, via the coupling to a cavity [29, 30] or a waveguide [13], only modest cyclicity ~ 15 has been achieved. The lack of intrinsically cyclic transitions in the Voigt configuration has prevented the simultaneous realization of both spin-selective readout and all-optical spin-control, and has been a major hurdle for QD systems vying for the realization of photonic quantum technologies.

In this work, we demonstrate quantum control of a QD electron-spin qubit in Faraday geometry – for both a GaAs QD and an InGaAs QD. A small light-hole admixture of the heavy-hole trion weakly breaks the full cyclicity of the spin-selective transitions, while maintaining it at a high value of 409 (289) for the GaAs (InGaAs) QD, and creates a highly asymmetric Λ system. Using a narrowband stimulated Raman scheme to drive electron-spin resonance [14], we account for the GHz-level differential Stark shifts arising from asymmetric Rabi frequencies in the Λ system, something otherwise impossible with broadband ps-pulse lasers [26]. With nuclear-spin stabilization of the qubit splitting, we narrow the electron spin resonance to 7(1) MHz (31(3) MHz), corresponding to a dephasing time of $T_2^* = 74(11)$ ns ($T_2^* = 17(2)$ ns) in a GaAs QD (an InGaAs QD) and achieve phase-tuneable control of the electron-spin qubit. With the GaAs QD, we achieve up to 273(6) MHz Rabi frequency and a π -pulse contrast of 97.4(1)%. We also perform nuclear-spin spectroscopy and demonstrate the compatibility of this control configuration with a nuclear quantum memory [17]. Our results demonstrate the technical feasibility of combining high-fidelity coherent control of QD spins and single-shot readout, with direct application to the deterministic generation of large entangled photonic states [32, 33].

Measurements presented in Figs. 1 and 6 are taken on both an InGaAs QD and a GaAs QD. Measurements presented in Figs. 2, 3, 4, and 5 are taken on a GaAs QD, while a subset of similar measurements performed on an InGaAs QD are presented in Appendix G.

II. DEVICES AND SPECTROSCOPY

We use two different QD devices in this work (Fig. 1a). The first consists of self-assembled InGaAs QDs emitting around 975 nm embedded in a Schottky diode (Device 1), while the second consists of droplet-etched GaAs QDs emitting around 775 nm embedded in a *p-i-n* diode (Device 2). Both devices are kept cold in a cryostat at 3.5-4.2 K, and are subject to a magnetic field up to $B_z = 8.0$ T applied along the growth axis (z) of the QDs. Details on the design of both devices can be found in Appendix B.

For both devices, we work with a single electron-charged QD, consisting of two Zeeman-split ground electron-spin states $|\downarrow\rangle$ and $|\uparrow\rangle$, and two excited negatively-charged exciton (trion) X^{1-} states $|\downarrow\downarrow\uparrow\rangle$ and $|\uparrow\downarrow\uparrow\rangle$. The trion hole states $|\uparrow\rangle$ and $|\downarrow\rangle$ consist predom-

inantly of heavy-hole (HH) states with a small admixture of light-hole (LH) states [34, 35] – as parametrized by the HH-LH admixture coefficient $\sigma_{lh}/\Delta_{lh} \equiv \epsilon_{lh} \ll 1$, where σ_{lh} parametrizes the off-diagonal coupling (in the Luttinger-Kohn Hamiltonian) – due to strain, disorder, or confinement effects – between LH and HH states and Δ_{lh} is the HH-LH energy splitting. The energy level schematic, depicted in Fig. 1(a), highlights the dominant circularly-polarized spin-conserving transitions $|\downarrow\downarrow\uparrow\rangle \leftrightarrow |\downarrow\downarrow\rangle$ and $|\uparrow\uparrow\uparrow\rangle \leftrightarrow |\uparrow\uparrow\rangle$ and the weaker spin-flipping transitions, $|\downarrow\downarrow\uparrow\rangle \leftrightarrow |\uparrow\uparrow\rangle$ and $|\uparrow\uparrow\uparrow\rangle \leftrightarrow |\downarrow\downarrow\rangle$. The spin-flipping transitions are forbidden for a pure HH X^{1-} states and weakly enabled in the presence of HH-LH admixture [36]. Depending on the exact nature of the LH mixing, the spin-flipping transitions can be linear π_z – i.e. along the growth, magnetic-field, and optical axes, and thus mostly dark [37] – or circularly polarized (see Appendix C). Despite the large strains present in InGaAs QDs, the spin-conserving HH transitions remain approximately cyclic due to the small QD sizes and thus to a large value of Δ_{lh} in the tens of meV [38]. However, the exact branching ratio between the spin-conserving and spin-flipping transitions can vary significantly across multiple QDs in the device due to the strain inhomogeneity of the Stranski-Krastanow growth process [35, 39]. The origin of the non-zero HH-LH admixture in a typically strain-free GaAs QD can be attributed to 3D confinement effects in nanostructures [40] – a smaller effective Δ_{lh} of ~ 3 meV together with small geometry- or disorder-induced effective shear strain components at the QD material interface [31].

Fig. 1(b, d) and Fig. 1(c, e) present the optical spectroscopy of the X^{1-} transition in an InGaAs QD (Device 1) and a GaAs QD (Device 2) at $B_z = 3.5$ T. Using a dark-field microscope [41], we scan across the X^{1-} resonance with a linearly polarized narrow-linewidth (~ 100 kHz) laser. The collected fluorescence from Device 1 (Device 2) is shown in Fig. 1(b) (Fig. 1(c)) as a function of device bias and laser frequency. At the edge of the charging plateau (device bias of ≈ 0.22 V and ≈ 0.30 V for Device 1 and device bias of ≈ 0.68 V and ≈ 0.87 V for Device 2), rapid tunneling of the electron from the QD to the diode back contact reservoir randomizes the spin states [42], thus preventing spin pumping and allowing us to observe steady-state fluorescence on resonance. In Device 1, we observe four distinct resonances: two strong and two weak transitions with relative intensities of approximately 100 : 1. This is consistent with the level diagram of Fig. 1(a), where the two strong (weak) transitions correspond to the spin conserving (flipping) transitions, and demonstrates that it is possible to directly excite the normally forbidden spin-flipping transitions. We further extract an electron-spin splitting of 30 GHz and a trion linewidth of 471(36) MHz from a Lorentzian fit to all four peaks at this bias. For Device 2, we observe only two sharp resonances, corresponding to the spin conserving transitions; this is likely due to the small

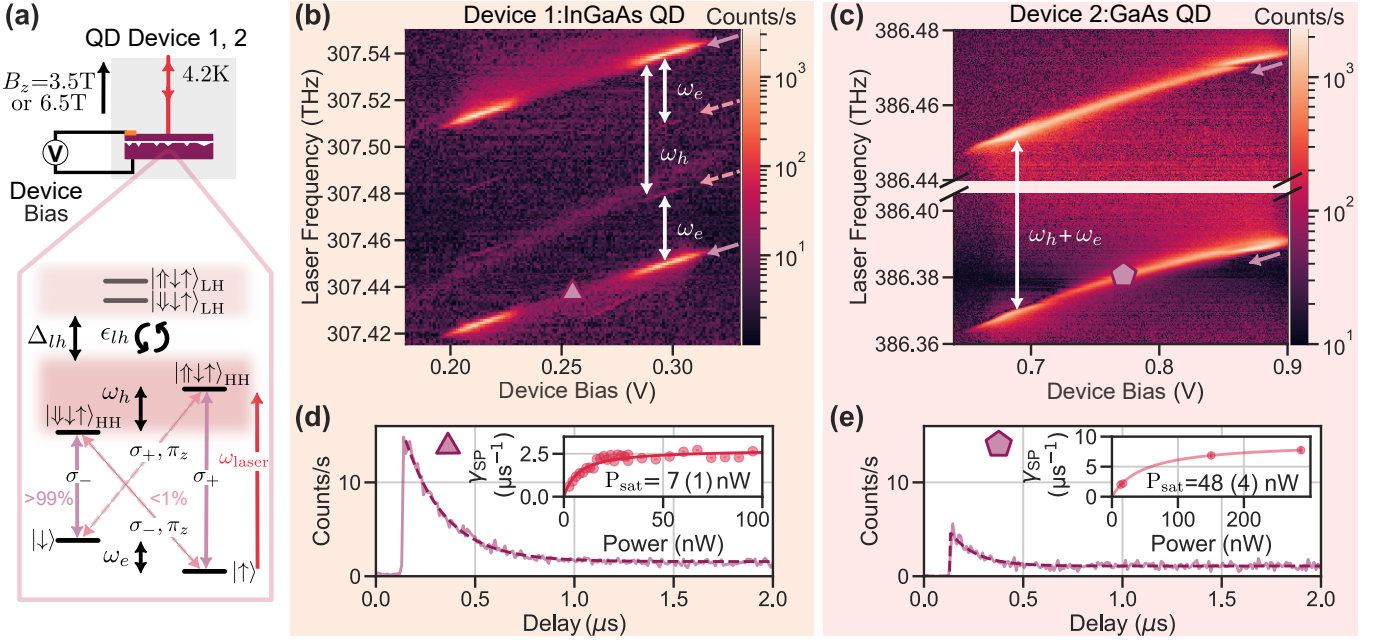


Figure 1. Optical Cyclicity of InGaAs and GaAs QDs in Faraday Geometry. (a) Top panel: schematic of experimental setup (further details in Appendix A) consisting of a charge-tuneable device, containing QDs, under an applied magnetic field B_z up to 6.5 T along the QD device growth axis z . A voltage bias V is applied to the Schottky (Device 1) or to the p-i-n (Device 2) diode to enable charge control and tuning of the emission energy via the d.c. Stark shift. Bottom panel: energy levels of a negatively-charged exciton X^{1-} in a Faraday field for a negative electron g -factor [31]. Solid purple arrows show the dominant circularly polarized dipole transitions connecting the electron-spin ground states, $|\downarrow\rangle$ and $|\uparrow\rangle$, to the heavy-hole (HH) trion states, $|\downarrow\downarrow\uparrow\rangle_{HH}$ and $|\uparrow\uparrow\uparrow\rangle_{HH}$, respectively. A small admixture (ϵ_{lh}) of the light hole (LH) X^{1-} states ($|\downarrow\downarrow\uparrow\rangle_{LH}$ and $|\uparrow\uparrow\uparrow\rangle_{LH}$), split to higher energy by Δ_{lh} , with the HH states enables the spin-flipping transitions (pink dashed arrows) to the two electron ground states. The branching ratio of the spin-conserving (spin-flipping) transitions is typically $> 99\%$ ($< 1\%$). (b) (c) Resonant spectroscopy of the X^{1-} of an InGaAs (GaAs) QD at $B_z = 3.5$ T with a linearly polarized narrow-linewidth laser at saturation power P_{sat} as a function of the Device bias V and laser frequency. The strong spin conserving transitions are highlighted by solid purple arrows, while the weaker spin-flipping transitions are highlighted by pink dashed arrows. For the InGaAs QD in Device 1, we extract an electron splitting $\omega_e = 30(1)$ GHz and a hole splitting $\omega_h = 59(1)$ GHz from Lorentzian fits to the resonances at a Device bias of 0.3 V. The combined electron and hole splitting is $\omega_e + \omega_h = 81.6(2)$ GHz for the GaAs QD in Device 2. (d) (e) Histogram of photon counts in a time-resolved pulsed resonant excitation experiment at a device bias of 0.26 V (0.78 V), showing optical spin pumping on the $|\downarrow\rangle \leftrightarrow |\downarrow\downarrow\uparrow\rangle$ transition at a power of 109 nW (287 nW). A decay time of 203(2) ns (111(1) ns) is obtained from an exponential fit (dashed curve). Insets show the spin pumping rate γ_{SP} (inverse of decay time) as a function of resonant laser power, where the solid curve is a fit of the data to a saturation model with parameter P_{sat} , resulting in $P_{sat} = 7(1)$ nW ($P_{sat} = 48(4)$ nW).

electron-spin splitting – a few GHz for GaAs QDs at this wavelength and field [31] – making the direct excitation of weak spin-flipping transitions difficult to resolve in close proximity to the strong spin-conserving transitions. The splitting between the two spin-conserving transitions reveals a combined electron and hole splitting of $\omega_h + \omega_e = 81.6(2)$ GHz. For this QD, we measure a trion linewidth of 851(27) MHz from a Lorentzian fit to the data taken at a device bias of 0.75 V and at zero field.

Focusing now on a device bias in the middle of the charging plateau, we observe a significantly lower intensity from the dominant peaks compared to that at the edge of the plateau (Fig. 1(b,c)). Despite the weakness of the spin flipping process in this field configuration (allowed by HH-LH mixing [31]), this measurement confirms the presence of significant optical pumping of the electron-spin population against background

spin relaxation mechanisms. A measurement of spin relaxation time T_1 , exceeding 40 μ s for both devices, is presented in Appendix B. We then probe the time scale of the spin-pumping process by measuring the time it takes for the electron spin to initialize to $|\uparrow\rangle$ by continuously driving the $|\downarrow\rangle \leftrightarrow |\downarrow\downarrow\uparrow\rangle$ transition for 5 μ s, shown in Fig. 1(d) and Fig. 1(e) for the two devices, respectively. Taken with a readout power exceeding 5 times the saturation power P_{sat} , to approach the minimum pumping time, our measurement reveals a fitted exponential decay time of $\gamma_{SP}^{-1} = 203(2)$ ns ($\gamma_{SP}^{-1} = 111(1)$ ns) for Device 1 (2), yielding the spin-flipping scattering rate γ_{SP} . Using the previously reported X^{1-} lifetime of $\gamma_1^{-1} \approx 0.7$ ns [43] for an InGaAs QD on this device and $\gamma_1^{-1} = 0.270$ ns [44] for a GaAs QD, we obtain an optical cyclicity of $\mathcal{C} \equiv \gamma_{SC}/\gamma_{SP} = \gamma_1/\gamma_{SP} - 1 = 289(3)$

and 409(6), where γ_{SC} is the spin-conserving scattering rate, and a branching ratio for the spin-flipping transition $\gamma_{\text{SP}}/\gamma_1$ [42, 45] of 0.34 % and 0.24 %, respectively. The cyclicity \mathcal{C} determines the mean number of photons scattered by the bright spin state before it flips to the dark spin state during a readout event, and sets the upper limit for the single-shot readout fidelity [46].

III. STIMULATED RAMAN TRANSITIONS IN FARADAY CONFIGURATION

Figure 2(a) shows the relevant energy levels involved in our spin control experiment. For readout, a resonant laser drives the lowest energy cycling transition $|\downarrow\downarrow\uparrow\rangle \leftrightarrow |\downarrow\rangle$ at $0.5 P_{\text{sat}} (\approx 25 \text{ nW})$ for both initialization to the spin $|\uparrow\rangle$ state and readout of the $|\downarrow\rangle$ state. To coherently control the ground state spin, we use an all-optical Raman drive that is circularly polarized and red-detuned by the single-photon detuning $\Delta \approx 600 \text{ GHz}$ from the $|\downarrow\downarrow\uparrow\rangle$ trion. The two Raman fields are derived from microwave-driven electro-optical modulation of a single narrow-band continuous-wave laser, resulting in a coherent pair of fields \vec{E}_\downarrow and \vec{E}_\uparrow equal in both intensity and polarization [27]. The two Raman fields, with resonant Rabi frequencies Ω_\downarrow and Ω_\uparrow , respectively, induce a rotation of the ground-state spin at a two-photon Rabi frequency $\Omega = \Omega_\downarrow\Omega_\uparrow/2\Delta$ when their frequency difference, the two-photon detuning ω , matches the ground-state splitting ω_e , i.e. achieving electron-spin resonance (ESR) at $\delta \equiv \omega - \omega_e = 0$. The small branching ratio of the spin-flipping transition implies a large imbalance in the Rabi frequencies of the two transitions – $\Omega_\downarrow \gg \Omega_\uparrow$ ($\Omega_\downarrow \ll \Omega_\uparrow$) for left-circularly (right-circularly) polarized Raman beams – which results in a large differential (a.c.) Stark shift $\Delta\delta \equiv \delta_\downarrow - \delta_\uparrow = (\Omega_\downarrow^2 - \Omega_\uparrow^2)/4\Delta$ on the electron-spin states during the Raman drive. We thus tune ω to match the ground state spin splitting $\omega_e = \omega_e^0 + \Delta\delta$, where ω_e^0 is the bare electron-spin splitting, and probe Raman resonance ($\omega \sim \omega_e$) when driven.

To visualize the effect of this imbalance, we can express the two-photon Rabi frequency Ω and the differential Stark shift $\Delta\delta$ in terms of Ω_\downarrow and the Rabi frequency imbalance, $\eta \equiv \Omega_\downarrow/\Omega_\uparrow$ as

$$\Omega = \frac{\Omega_\downarrow\Omega_\uparrow}{2\Delta} = \frac{\Omega_\downarrow^2}{2\eta\Delta} \quad (1)$$

and

$$|\Delta\delta| = \frac{|\Omega_\downarrow^2 - \Omega_\uparrow^2|}{4\Delta} = \Omega \frac{\eta^2 - 1}{2\eta}, \quad (2)$$

respectively. In the situation where the two Raman fields have equal intensity, $|\vec{E}_\downarrow|^2 = |\vec{E}_\uparrow|^2$, and are exactly matched to two transition dipoles \vec{d}_\downarrow and \vec{d}_\uparrow (i.e. the expectation value of the electric dipole Hamiltonian $\langle \vec{d} \cdot \vec{E} \rangle$ is maximized),

$$\begin{aligned} \eta^2 &= \left(\frac{\Omega_\downarrow}{\Omega_\uparrow} \right)^2 = \left(\frac{\langle \vec{d}_\downarrow \cdot \vec{E}_\downarrow \rangle}{\langle \vec{d}_\uparrow \cdot \vec{E}_\uparrow \rangle} \right)^2 \\ &\rightarrow \left(\frac{|\vec{d}_\downarrow|}{|\vec{d}_\uparrow|} \right)^2 = \frac{\gamma_{\text{SC}}}{\gamma_{\text{SP}}} = \mathcal{C}, \end{aligned} \quad (3)$$

(or $= \gamma_{\text{SP}}/\gamma_{\text{SC}} = \mathcal{C}^{-1}$) for left-circular (right-circular) polarization. As such, using our cyclicity of $\mathcal{C} = 409$, we can expect a shift in the ESR resonance by 10Ω . At a typical Rabi frequency of $\Omega = 100 \text{ MHz}$, this corresponds to a shift of $|\Delta\delta| = 1 \text{ GHz}$, which exceeds even the inhomogeneous ESR linewidth ($\sim 300 \text{ MHz}$ [14, 18, 47]).

As we are unable to resolve the electron splitting via spectroscopy for the GaAs QD in Device 2 (Fig. 1(c)), we perform two-laser resonant spectroscopy at a fixed bias of 0.775 V and a magnetic field of 6.5 T with a fixed pump laser frequency at 386.435 THz while varying the frequency of a second probe laser. The pump and probe laser powers are fixed at approximately $14 P_{\text{sat}}$ and $1.4 P_{\text{sat}}$, respectively. The resulting steady-state fluorescence data is shown in Fig. 2(b) and shows a dip in the signal, a signature of coherent population trapping (CPT) [48–50], when the two lasers meet the two-photon resonance condition for the spin conserving and spin flipping transitions. Following a fit to the measurement data using the model and parameters described in Appendix H, the dip minimum reveals a bare electron splitting of $\omega_e^0 = 2.60(1) \text{ GHz}$ – corresponding to an out-of-plane g -factor of 0.0286(1), as consistent with previous measurements [31].

Finding the ESR frequency in a Raman experiment requires stabilizing the Overhauser shift imparted by nuclear spins on the electron-spin splitting [14]. We do this using nuclear-spin cooling techniques – one of Raman [14], Rabi [47], or quantum-algorithmic [25] cooling, depending on the experiment. Our typical pulse sequence, shown in Fig. 2(c), consists of a cooling period – during which our coherent Raman drive and resonant readout serve to sense and correct the nuclear polarization – followed by a probe experiment (representing $\sim 10\%$ of the duty cycle) in which the electron spin is initialized, driven coherently by Raman beams for a fixed duration, and read out. Fixing the probe Rabi frequency to $\Omega \approx 110 \text{ MHz}$ and the pulse duration to $\tau = 1/(2\Omega) = 4.5 \text{ ns}$, i.e. π pulse, we measure the readout fluorescence as a function of probe frequency ω – here the Raman cooling frequency ω_{cool} is also set to ω . We observe a clear electron-spin resonance (ESR) signal shifted from ω_e^0 by about $\sim 1 \text{ GHz}$ (2 GHz) down (up) for left-circularly (right-circularly) polarized Raman light. The sign of the shift matches our expectation as a red-detuned beam lowers the energy of the ground state; here, the stronger spin-conserving left-circularly (right-circularly) polarized transition lowers the \downarrow (\uparrow) state more than the spin-flipping transition lowers the state \uparrow (\downarrow), resulting in a decrease (an increase) in

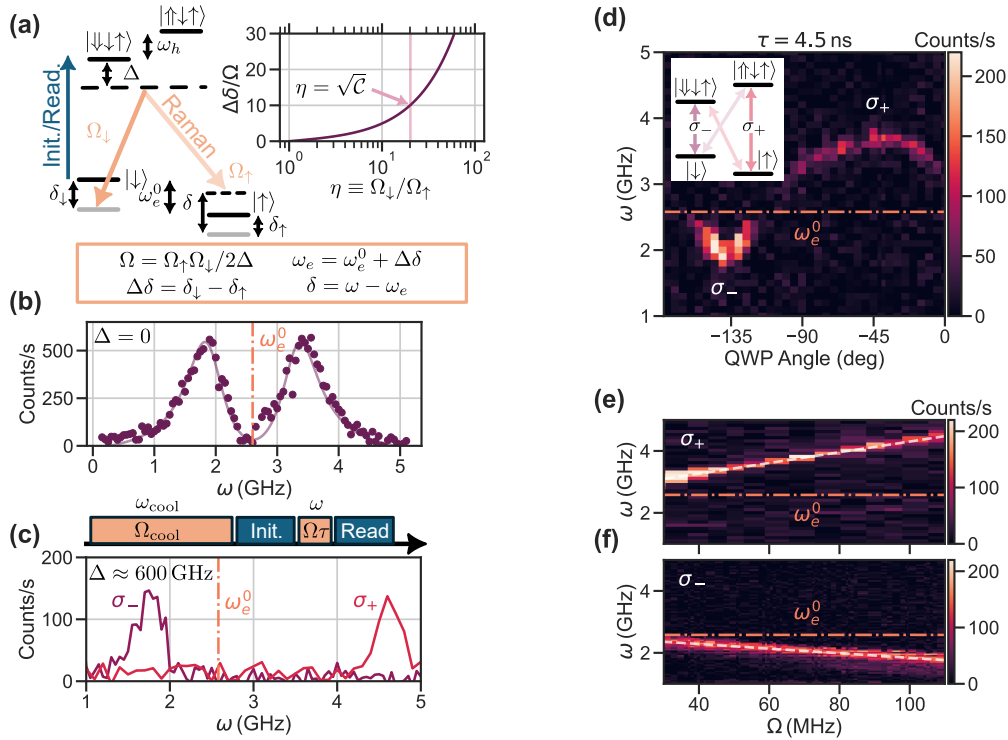


Figure 2. Dependence of electron spin resonance on Raman laser at $B_z = 6.5$ T. All measurements are taken on a GaAs QD in Device 2. **(a)** Energy levels relevant for spin control. The initialization/readout laser (blue arrow) is resonant with transition $|\downarrow\downarrow\uparrow\rangle \leftrightarrow |\downarrow\uparrow\rangle$. The Raman fields (orange arrows) with Rabi frequency Ω_\downarrow and Ω_\uparrow are detuned by $\Delta \approx 600$ GHz from the lower-energy trion and couple the two ground states $|\downarrow\rangle$ and $|\uparrow\rangle$, respectively, at a two-photon Rabi frequency Ω . Each Raman field exerts an a.c. Stark shift (gray lines) δ_\downarrow and δ_\uparrow on its respective ground state, resulting in a differential Stark shift $\Delta\delta$. The right panel shows the ratio of the differential Stark shift and two-photon Rabi frequency, $\Delta\delta/\Omega$, as a function of the Rabi frequency imbalance $\eta = \Omega_\downarrow/\Omega_\uparrow$, related to cyclicity in the ideal scenario by $\eta = \sqrt{C}$. **(b)** Continuous two-color resonant ($\Delta = 0$) measurement with a fixed-frequency laser (pump) set to 700 nW ($\approx 14 P_{\text{sat}}$) and a variable frequency laser (probe) set to 70 nW ($\approx 1.4 P_{\text{sat}}$). The resulting fluorescence signal is shown as a function of relative pump-probe (two-photon) detuning ω . A fit (solid curve) to the data with a three-level model (see Appendix H) reveals an electron-spin splitting of $\omega_e^0 = 2.60(1)$ GHz from the dark-state (dip) resonance condition $\omega = \omega_e^0$. **(c)** Top: pulse sequence for obtaining an ESR spectrum consisting of nuclear-spin cooling (Rabi cooling) at Rabi frequency $\Omega_{\text{cool}} = \Omega$ and drive frequency $\omega_{\text{cool}} = \omega$ followed by spin initialization, a short probe with Rabi frequency Ω , drive frequency ω and duration τ , and a spin readout. Bottom: readout fluorescence as a function of drive frequency. Measurements are performed at $\Omega \approx 110$ MHz and $\tau = 4.5$ ns using the Raman laser polarization settings aligned to σ_- (purple data) and σ_+ (red data). **(d)** ESR spectrum as a function of Raman laser polarization set by the quarter-wave-plate (QWP) angle. QWP angle of 0° is calibrated to correspond to linear horizontal polarization, and the right-hand (σ_+) and left-hand (σ_-) circular polarizations are at -45° and -135° , respectively. **(e)** **(f)** ESR spectrum as a function of Rabi frequency for right-hand (left-hand) circular polarization. Dashed lines are linear fits to the frequency corresponding to a fluorescence maximum, with fitted slopes $-7.4(5)$ and $17.2(6)$. Both fits converge to $\omega_e^0 = 2.58(3)$ GHz at the limit of vanishing Ω .

the electron-spin splitting that is proportional to the Raman laser intensity.

Fig. 2(d) shows a summary of this measurement as a function of the angle of the quarter-wave plate (QWP) used to tune the circularity of the Raman laser, where 0° is calibrated to correspond to linear horizontal polarization. We observe clearly that the Raman laser must exhibit a well defined handedness for ESR to be possible. Moreover, the maximal amplitude and maximally-positive and negative shifts in the ESR resonance occur at -45° and -135° , respectively, corresponding to σ_+ and σ_- polarization settings and matching the dipoles of the two spin-conserving transitions (further details

in Appendix D). This implies destructive interference of the two Λ systems when driving with linearly polarized light, which is expected for a specific kind of HH-LH mixing as shown in Appendix C – by contrast, on the In-GaAs QD in Device 1 a degree of linear diagonal polarization seems to improve the Raman coupling (see Appendix G), which would imply a different kind of HH-LH mixing. We further observe a larger maximal shift from the undriven resonance frequency ω_e^0 (horizontal dashed line) for σ_+ than for σ_- and a clear deviation from a simple sinusoidal dependence on QWP angle. While we expect a small difference in coupling between σ_+ and σ_- polarizations, due to the trion splitting mak-

ing the Raman detuning for σ_+ larger by $\omega_h \approx 150$ GHz, this asymmetric response to σ_+ and σ_- suggests an additional mechanism is present.

Fig. 2(e,f) shows a summary of ESR measurements now taken as a function of probe Rabi frequency Ω , for right-circular (e) and left-circular polarization (f). We observe a clear linear dependence on Ω of the ESR peak frequency $\omega_e = \omega_e^0 + \Delta\delta$, as expected from Eqn. 2. Fitting ω_e as a function of Ω with two independent linear functions, we obtain $\Delta\delta/\Omega = 17.2(6)$ and $\Delta\delta/\Omega = -7.4(5)$, corresponding to Rabi frequency imbalances of $\eta = 34(1)$ and $\eta = 15(1)$, respectively, and an undriven resonance frequency $\omega_e^0 = 2.58(3)$ GHz that agrees closely between the two linear fits (and is within one standard error of our CPT result in Fig. 2(b)). These values of η deviate measurably from the idealized value derived from our measured optical cyclicity $\eta = \sqrt{C} = 20.2(1)$, which implies some polarization and spatial mode mismatch between the Raman beams and the transition dipole moments of both spin-conserving and spin-flipping transitions (see Eqn. 3). Equations 1 and 2 tell us that the differential light shift is dominated by the spin-conserving transition Rabi frequency Ω_\downarrow (Ω_\uparrow) for σ_- (σ_+), whereas the two-photon Rabi frequency Ω is equally affected by the spin-conserving and spin-flipping contributions. The unequal response of the ESR frequency as a function of Rabi frequency between σ_+ and σ_- polarizations thus reveals that the Raman beam coupling to the spin-flipping transition must differ significantly between the two polarization settings. A possible explanation is that minor alignment differences could result in a larger coupling to the π_z component of the LH transition for σ_- , thus enhancing the Raman coupling Ω for this configuration.

The results in Fig. 2 highlight the essence of optical spin control in the Faraday configuration: an inevitable shift in the ESR frequency that depends on Raman laser polarization and the instantaneous Rabi frequency, which must be calibrated, as we have done, before experiments with programmable pulse amplitude and phase can be performed.

IV. RABI OSCILLATIONS AND QUALITY FACTOR

With the stabilization of the ESR and the calibration of the differential Stark shift achieved, we proceed to show time-resolved coherent driving of the electron spin on resonance. For that, we measure the readout counts as a function of probe pulse duration following stabilization of the nuclei via Raman cooling, as depicted in Fig. 3(a). The resulting signal shows damped Rabi oscillations when the ESR drive is resonant ($\delta = 0$). When the detuning is increased to $\delta = 400$ MHz, we observe a monotonic increase in bright-state population once a few detuned Rabi oscillations have decohered ($\tau \gtrsim 30$ ns); an exponential fit yields a relaxation rate of $\Gamma_1/2\pi = 0.8(2)$ MHz and provides a di-

rect measurement of background optically induced spin relaxation [27]. The purple solid curve is a fit to a master equation model (see Appendix I) accounting for the measured inhomogeneous broadening of 14 MHz ($T_2^* = 34$ ns), the measured spin relaxation rate Γ_1 , and spin dephasing with a free parameter Γ_2 . From this fit, we extract a Rabi frequency of $\Omega = 226.8(3)$ MHz (or a π -time of $t_\pi = 1/2\Omega = 2.195(2)$ ns) and spin dephasing rate of $\Gamma_2/2\pi = 3.7(1)$ MHz. From the fitted density matrix, we also extract a π -pulse contrast of 96.8(1)%, which is an upper bound on the π -pulse fidelity [27], and a corresponding Rabi oscillation quality factor $Q = -1/\ln(2f_\pi - 1) = 15.1(6)$.

Fig. 3(b) and (c) shows the quality factor Q and spin dephasing rate Γ_2 , extracted from our master equation model as in Fig. 3(a), as a function of probe Rabi frequency Ω . Our optimal factor of $Q = 18.8(3)$, corresponding to a π -pulse contrast of 97.4(1)%, is obtained for $\Omega = 217(5)$ MHz. The overall increase in Q towards this value is expected from previous work [27, 47], where Rabi frequencies well beyond $(2\pi T_2^*)^{-1}$ and nuclear Zeeman frequencies (50 – 80 MHz) enable decoupling from nuclear effects. This behavior is also reflected in our fitted Γ_2 values, which start out low due to inhomogeneity-dominated dephasing at low Ω , peak at 4 – 6 MHz around $\Omega = 50$ MHz (i.e. the Arsenic nuclear Larmor frequency) and taper off to 2 – 4 MHz at higher Ω values. The subsequent decrease in Q and increase in Γ_2 for $\Omega \gtrsim 230$ MHz, however, is likely due to a mechanism made worse by Faraday-geometry spin control: laser intensity noise. Any fluctuation in Raman laser intensity not only changes the instantaneous Rabi frequency but also the electron-spin splitting directly via the differential Stark shift. As Ω scales linearly with laser intensity, \mathcal{I} , we can determine the fluctuation in the ESR shift as $d(\Delta\delta)/\Delta\delta = d\mathcal{I}/\mathcal{I}$. In the experiment, we measured a typical laser power fluctuation $\sim 1\%$ (integrated over the full bandwidth of our photo-detector) that worsened at our maximum laser intensities. With a differential Stark shift of $\Delta\delta = -7.4(5)\Omega$ (see Fig. 2(f)), $\Omega = 250$ MHz would result in a broadening of the ESR resonance $d(\Delta\delta) \lesssim 18.5$ MHz. While our fitted dephasing rate of $\Gamma_2/2\pi = 8 - 10$ MHz for $\Omega \approx 250$ MHz is significantly lower than this bound, this could be explained by a partial decoupling from the noise spectrum below Ω in a resonant Rabi experiment [27]. To verify this further, we artificially introduce broadband intensity noise (up to 35 MHz) on the Raman laser and measure the resulting Rabi oscillations. The summary is shown in Fig. 3(d) and (e), where a steady decrease of Q and a steady increase of Γ_2 , respectively, as a function of $d\mathcal{I}/\mathcal{I}$ can be observed for $d\mathcal{I}/\mathcal{I} \gtrsim 0.025$. These behaviors are qualitatively matched by our master equation model (see Appendix E), which treats the added intensity noise as a source of inhomogeneity.

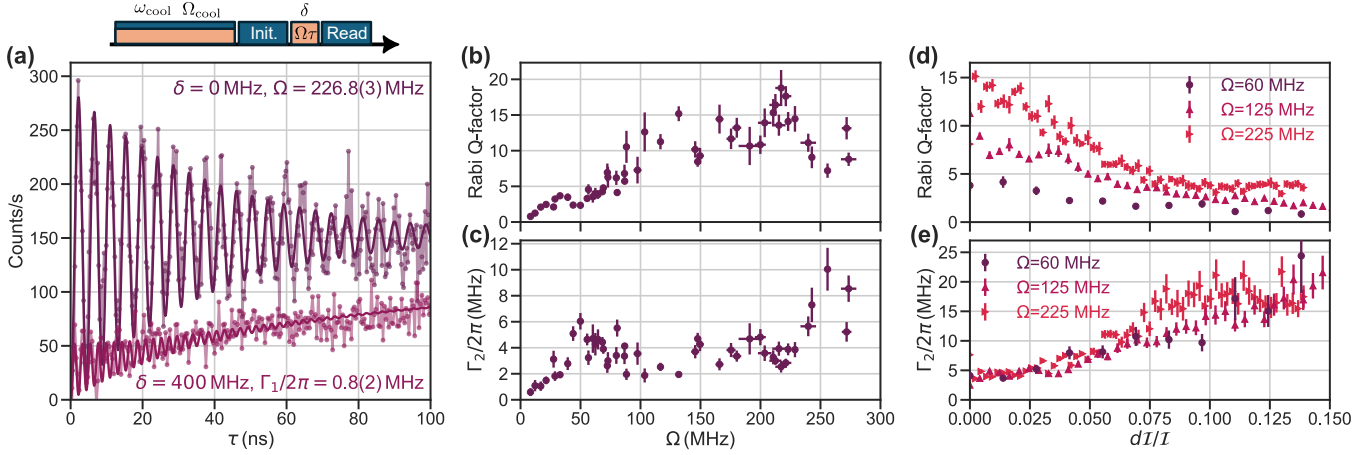


Figure 3. **Coherent control of the electron spin.** All measurements are taken on a GaAs QD in Device 2. **(a)** Measurement of Rabi oscillations with pulse sequence (top) consisting of nuclear-spin cooling (Raman cooling) at Rabi frequency Ω_{cool} and drive frequency ω_{cool} followed by spin initialization, a probe pulse with Rabi frequency Ω , detuning δ and duration τ , and a spin readout. Measurement data is readout counts as a function of τ , and shows Rabi oscillations at $\delta = 0$ and laser-induced spin relaxation at $\delta = 400$ MHz. The solid curves are a master equation model (Appendix I), with fixed $T_2^* = 34$ ns, used to fit the relaxation rate $\Gamma_1/2\pi = 0.8(2)$ MHz at $\delta = 400$ MHz and the Rabi frequency $226.8(3)$ MHz and dephasing rate $\Gamma_2/2\pi = 3.7(1)$ MHz at $\delta = 0$ MHz. The Rabi quality factor is $Q = 15.1(6)$. **(b)** Rabi quality factor Q and **(c)** spin dephasing rate $\Gamma_2/2\pi$ as a function of Ω for $\Omega_{\text{cool}} = 15$ MHz. **(d)** Rabi quality factor Q and **(e)** spin dephasing rate $\Gamma_2/2\pi$ as a function of artificially-introduced Raman laser intensity modulation dI/I at three probe Rabi frequencies Ω . Error bars indicate one standard error on fitted parameters.

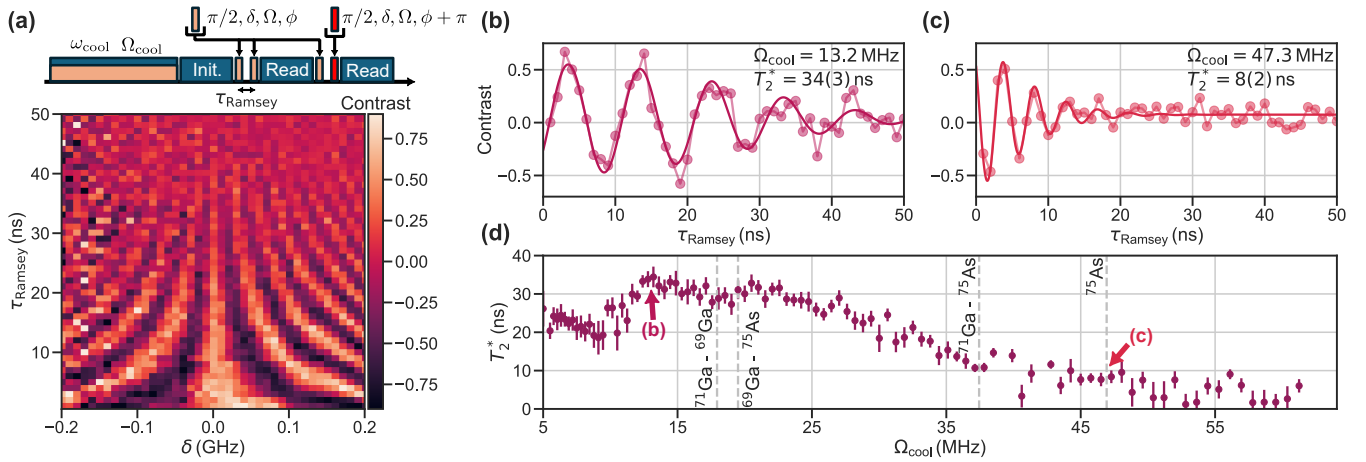


Figure 4. **Phase-resolved control of the electron-spin qubit.** All measurements are taken on a GaAs QD in Device 2. **(a)** Ramsey measurement with pulse sequence (top) consisting of nuclear-spin cooling (Raman cooling) at Rabi frequency Ω_{cool} and drive frequency ω_{cool} followed by two Ramsey sequences. The first Ramsey sequence consists of spin initialization, a first $\pi/2$ rotation with phase ϕ (i.e. our phase reference), a Ramsey delay time τ_{Ramsey} , a second $\pi/2$ rotation with phase ϕ , and a spin readout with average count n_ϕ . The second Ramsey sequence consists of spin initialization, a first $\pi/2$ rotation with phase ϕ , a Ramsey delay time τ_{Ramsey} , a second $\pi/2$ rotation with phase $\phi + \pi$, and a spin readout with average count $n_{\phi+\pi}$. Our signal is the contrast $(n_\phi - n_{\phi+\pi}) / (n_\phi + n_{\phi+\pi})$. All rotations are performed with $\Omega = 125$ MHz and a detuning δ . Measurement data shows contrast as a function of δ and τ_{Ramsey} for $\Omega_{\text{cool}} = 15$ MHz. **(b)** **(c)** Contrast as a function of τ_{Ramsey} for $\Omega_{\text{cool}} = 13.2$ MHz ($\Omega_{\text{cool}} = 47.3$ MHz). The solid curve is a fitting function $A \sin(2\pi\delta\tau_{\text{Ramsey}} + \theta) \exp(-(\tau_{\text{Ramsey}}/T_2^*)^2)$ with free parameters: A as a contrast amplitude, δ as the detuning from ESR, θ as a phase, and T_2^* as the characteristic decay time. The relevant fit results are $T_2^* = 34(3)$ ns ($T_2^* = 8(2)$ ns) and $\delta = 100(1)$ MHz ($\delta = 229(4)$ MHz). **(d)** Inhomogeneous dephasing time T_2^* , fitted from Ramsey experiments as performed in (b,c), as a function of Ω_{cool} . Dashed lines highlight expected single- and double-species nuclear resonances within this range of frequencies. Error bars indicate one standard error on fitted parameters.

V. QUANTUM CONTROL AND COHERENCE

Next we demonstrate complete control over the electron-spin qubit by performing phase-modulated Ramsey interferometry. Our sequence, shown in Fig. 4(a), consists of a balanced readout using two sequences, one with and one without an extra π phase on the second $\pi/2$ pulse, which follows a delay time τ_{Ramsey} from a first $\pi/2$ pulse. The readout counts are given by n_ϕ and $n_{\phi+\pi}$, respectively, where ϕ is the pulse phase, and our signal is then the contrast $(n_\phi - n_{\phi+\pi})/(n_\phi + n_{\phi+\pi})$. Fig. 4(a) shows the Ramsey contrast as a function of drive detuning δ and Ramsey delay τ_{Ramsey} , displaying the expected chevron pattern in the presence of sufficient coherence to observe clearly resolved fringes.

To measure the inhomogeneous dephasing time T_2^* we take the Ramsey data at a finite detuning δ from ESR, corresponding to a Ramsey-delay-dependent phase $\phi + 2\pi\delta\tau_{\text{Ramsey}}$ on the second $\pi/2$ pulse (ϕ as our phase reference for the first pulse), and thus contrast oscillations at a frequency δ to enable better fitting to the decay envelope. This is shown in Fig. 4(b), where we extract $T_2^* = 34(3)$ ns from a Gaussian envelope fit with $\delta = 100(1)$ MHz. As known from previous work [14], the dephasing time T_2^* depends on the cooling Rabi frequency Ω_{cool} – as shown by a striking decrease to $T_2^* = 8(2)$ ns for $\Omega_{\text{cool}} = 47.3$ MHz (Fig. 4(c)). A full summary of the dependence of T_2^* on Ω_{cool} is shown in Fig. 4(d), where the optimal cooling performance is found for $\Omega_{\text{cool}} \sim 15$ MHz. This is consistent with previous results in the Raman cooling configuration, where the optimal cooling Rabi frequency was a fraction of the nuclear Zeeman frequency [14].

VI. ORIGINS OF NUCLEAR COOLING

To probe the nature of the electro-nuclear interaction, we run nuclear-magnon spectroscopy [14], which consists of a Rabi probe sequence where the drive detuning and duration are varied, while the drive Rabi frequency is fixed to $\Omega = 6$ MHz. The results are shown in Fig. 5(a) and Fig. 5(b), where at $\delta \approx 0$ we observe our typical ESR signal and Rabi oscillations, with a full-width at half-maximum of $7(1)$ MHz consistent with $T_2^* = 74(11)$ ns – obtained with modified quantum algorithmic cooling (see Appendix F). At a finite detuning $\delta \approx 47$ MHz, which matches the Arsenic (As) Larmor frequency, we see another resonance appear, corresponding to a magnon mode of that species. Less pronounced resonances at $\delta \approx 67$ MHz and $\delta \approx 85$ MHz likely correspond to the two Gallium isotopes, ^{69}Ga and ^{71}Ga . This confirms our ability to excite nuclear magnon modes in this Faraday configuration, as a first step towards a quantum memory [17].

The presence of nuclear resonances is further confirmed by performing Hahn Echo spectroscopy [51, 52],

where our probe sequence consists of the addition of a refocusing π pulse half-way between the Ramsey pulses of Fig. 4(a). Fig. 5(b) shows the contrast as a function of total delay time T . The overall decaying contrast as a function of T is fitted to a Gaussian function to extract the electron-spin qubit decoherence time $T_2^{\text{HE}} = 1.14(2)$ μs – shorter than previous results on GaAs [16, 18], which is consistent with a stronger interaction with the transverse nuclear field owing to a QD whose physical size is smaller (blue-shifted [31]) and whose electron-spin splitting ω_e^0 is smaller. Zooming in on short delays, shown in the inset of Fig. 5(b), we see oscillations of the contrast, which a Fourier transform of the signal, shown in Fig. 5(c), confirms to be predominantly at the As Larmor frequency. These Hahn Echo oscillations and the magnon resonances are features of an interaction between the electron spin and a precessing transverse nuclear field [16, 53], which allows the electro-nuclear energy exchange required for nuclear-spin cooling [25] and quantum gates between the electron-spin qubit and a nuclear magnon [17].

For an InGaAs QD, strain produces a large misalignment of nuclear and electronic quantization axes that, independently of the magnetic field direction due to strain inhomogeneity, naturally leads to a *non-collinear* hyperfine interaction [54] as used in cooling [14]. However, for a strain-free GaAs QD subject to a growth-axis magnetic field, the electronic and nuclear quantization axes should be fully aligned and there should not be a significant non-collinear interaction. Instead, the small electron-spin splitting $\omega_e^0 = 2.6$ GHz makes the transverse *collinear* interaction, whose amplitude scales as ω_e^{-1} , sufficiently strong to be observed here. A hallmark of this interaction is that it enables only spin-conserving processes and thus only a single sideband in the ESR spectrum – unlike the non-collinear interaction, which allows bidirectional sideband processes [14, 54]. This single sideband is precisely what we observe in Fig. 5b, where its blue-detuning ($\delta > 0$) is seen to be independent of the probe electron-spin state as consistent with a single spin-conserving process.

VII. CONTROL OF QD SPINS

Lastly, we offer a succinct performance overview of InGaAs (Device 1) and GaAs (Device 2) QDs in Fig. 6, where Rabi oscillations and laser-induced relaxation rate (at the same Rabi frequency), and Ramsey interferometry are shown side-by-side. Laser-induced relaxation – which we know from previous work to be purely power-dependent and not related to scattering from the trion [27, 55] – is measured as a function of Raman laser power and fitted to $0.131(2)$ $\mu\text{s}^{-1}/\mu\text{W}$ for Device 1 (which is $\sim 25\%$ of what was previously measured on the same wafer [27]) and to $0.026(2)$ $\mu\text{s}^{-1}/\mu\text{W}$ for Device 2, which is to the best of our knowledge the low-

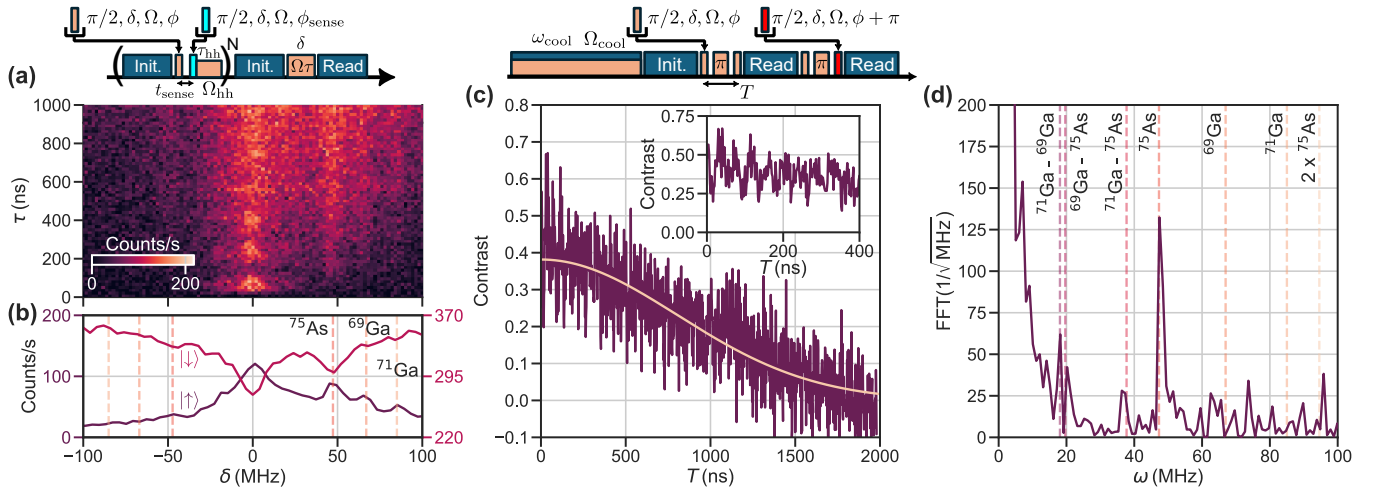


Figure 5. Nuclear-magnon and Hahn-Echo spectroscopy. All measurements are taken on a GaAs QD in Device 2. **(a)** Nuclear-magnon spectroscopy measurement with pulse sequence (top panel) consisting of nuclear-spin cooling (modified quantum algorithmic cooling; see Appendix F) at Rabi frequency $\Omega_{\text{hh}} = 47$ MHz followed by a probe Rabi sequence consisting of spin initialization, a Rabi drive at Rabi frequency $\Omega = 6$ MHz, detuning δ , and of duration τ , and spin readout. The color map shows the resulting average readout counts as a function of δ and τ . **(b)** Spectrum, acquired as in (a), averaged over all Rabi drive durations when the electron spin is initialized to $|\uparrow\rangle$ (purple), as in (a), or to $|\downarrow\rangle$ (pink), with an additional π pulse before the Rabi drive; the readout remains on the $|\downarrow\rangle$ state. **(c)** Hahn Echo spectroscopy measurement with pulse sequence (top) consisting of the same pulse sequence as in Fig. 4a with the addition of refocusing π pulses halfway between the Ramsey pulses. The resulting contrast as a function of total delay time T is shown below. The solid curve is a fit to the function $A \exp(-(T/T_2^{\text{HE}})^2)$, where $T_2^{\text{HE}} = 1.14(2) \mu\text{s}$ and A is the amplitude of the envelope. Inset: zoom in of the same data. **(d)** Fourier transform of the data in (c). Dashed lines are expected nuclear Larmor frequencies. Data in (c) and (d) is taken at a cooling frequency $\omega_{\text{cool}} = 2.3$ GHz.

est value reported for any InGaAs or GaAs spin-control experiment. While the lower rate of laser-induced relaxation for Device 2 is a contributor to higher quality Rabi oscillations, the dominant dephasing mechanism for both devices is a T_2 process that likely arises in part from laser intensity noise coupled in via the differential Stark effect.

For Device 1, our best Rabi oscillations reach $\Omega = 66(7)$ MHz and $Q = 0.90(8)$, and our best measured coherence is $T_2^* = 17(2)$ ns with quantum-algorithmic cooling (further details in Appendix G). For Device 2, our best Rabi oscillations reach $\Omega = 273(6)$ MHz and $Q = 18.8(3)$, and our best measured coherence is $T_2^* = 74(11)$ ns with quantum-algorithmic cooling – in this case we adapted the cooling algorithm to use the transverse collinear interaction, as further described in Appendix F. While it is tempting to make conclusions about InGaAs vs GaAs QDs on this basis, it is unclear what leads to the striking difference in performance measured here – it may simply be a difference in the optical quality of the QD heterostructure rather than a difference intrinsic to InGaAs vs GaAs QDs.

VIII. CONCLUSIONS

With this, we have demonstrated full quantum control of an electron-spin qubit in Faraday geometry for both InGaAs and GaAs QDs, where the cyclicity of spin

readout transitions was measured to be $\mathcal{C} = 289$ and $\mathcal{C} = 409$, respectively. As compared with the state-of-the-art in Voigt geometry of $T_2^* > 600$ ns [47] and $Q = 45$ [17] on an electron spin in a GaAs QD, we attribute the lower spin coherence and rotation fidelity to the coupling of the qubit splitting to laser intensity fluctuations via the differential Stark shift and to the increased relative importance of laser-induced relaxation in the presence of a weaker spin-flipping transition. Further improvements include stabilizing the laser intensity at the QD position to better than 0.1% via vibration isolation and optimized power stabilization. Additionally, applying a vectorial magnetic field (i.e. a combination of Faraday and Voigt configurations) or controlled strain to increase HH-LH mixing (on a GaAs QD [56]) would increase the strength of the spin-flipping transition and reduce the induced differential Stark shift, while keeping the cyclicity sufficiently high for single-shot readout. Single-shot measurements are not currently possible in our system due to a low end-to-end efficiency of less than 1% after propagating through the microscope, optical filters, and single-photon detector. With a cyclicity of ≈ 400 , an improvement to $\sim 10\%$ efficiency would suffice, made straightforward by photonic structures now reaching 70% end-to-end efficiency with similar QDs [12, 57, 58], which combined with our method would allow for the generation of photonic cluster states with tens to hundreds of photons.

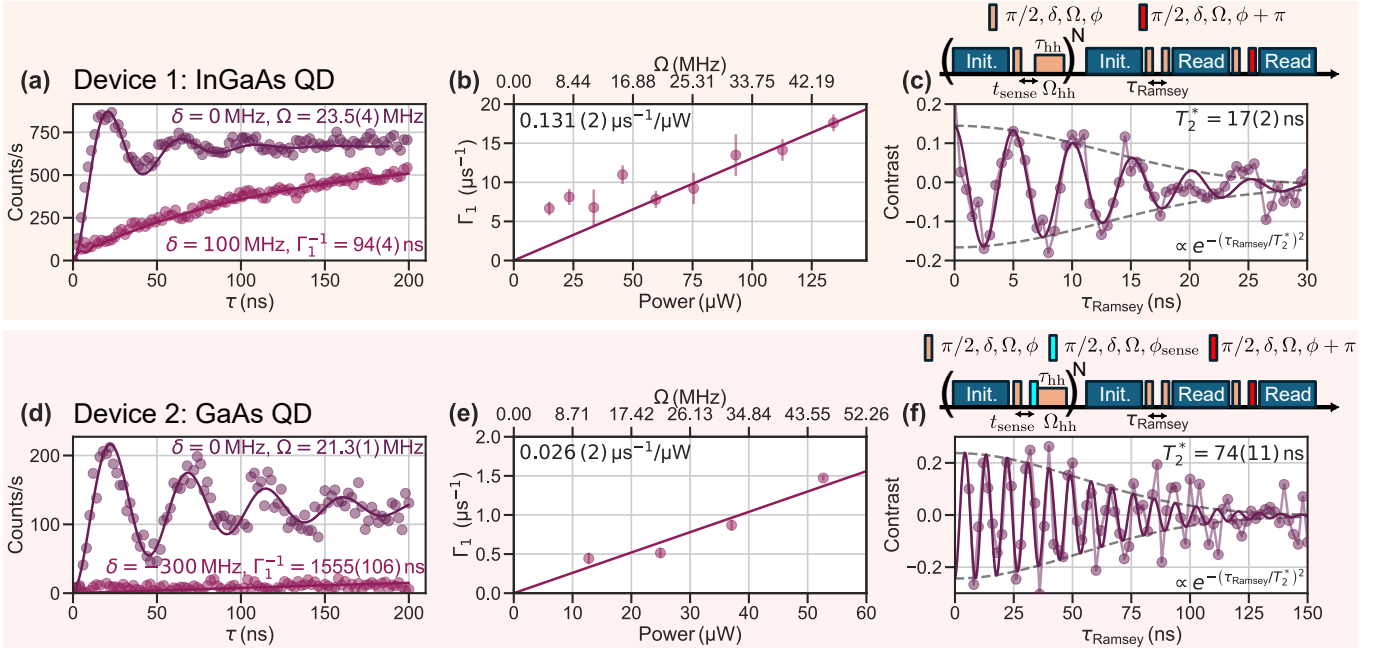


Figure 6. **Faraday quantum control of an electron-spin qubit in an InGaAs QD and a GaAs QD.** (a - c) ((d - f) are data for an InGaAs QD in Device 1 (a GaAs QD in Device 2). Details on quantum-algorithmic cooling used with Device 1 can be found in Appendix G. (a) ((d)) Using the pulse sequence in Fig. 3a with quantum-algorithmic cooling (Raman cooling), Rabi oscillations at $\delta = 0$ and laser-induced relaxation at $\delta = 100$ MHz ($\delta = -300$ MHz). Solid curves are from our master equation model (Appendix I) from which we fit $\Omega = 23.5(4)$ MHz ($\Omega = 21.3(1)$ MHz) and $\Gamma_1^{-1} = 94(4)$ ns ($\Gamma_1^{-1} = 1555(106)$ ns). (b) ((e)) Γ_1 as a function of Raman laser power. The solid line is a linear fit (no offset) with slope $0.131(2)\mu\text{s}^{-1}/\mu\text{W}$ ($0.026(2)\mu\text{s}^{-1}/\mu\text{W}$). (c) ((f)) Our pulse sequence consists of quantum-algorithmic cooling, which for Device 2 (f) is adapted to the transverse collinear interaction by adding a $\pi/2$ pulse with a phase ϕ_{sense} (see Appendix F). This is followed by a Ramsey measurement as done in Fig. 4 but with a serrodyne frequency $f_{\text{serr}} = 200$ MHz (100 MHz) applied to the second Ramsey pulse. The data show Ramsey contrast as a function Ramsey delay τ_{Ramsey} . The solid curve is a fitting function $A \sin(2\pi f \tau) \exp(-(\tau/T_2^*)^2)$ with free parameters: A as the contrast amplitude, $f \approx f_{\text{serr}}$ as the contrast oscillation frequency, and T_2^* as the characteristic decay time. The fit results are $T_2^* = 17(2)$ ns ($T_2^* = 74(11)$ ns), $f = (197(2)$ MHz ($f = 112(1)$ MHz). Error bars indicate one standard error on fitted parameters.

ACKNOWLEDGMENTS

We acknowledge support from an EPSRC New Investigator Award EP/W035839/2 (D.A.G., Z.X.K.), the QuantERA project MEEDGARD through EPSRC EP/Z000556/1 (D.A.G., M.A.), ETRI through The Institute of Information & communications Technology Planning & Evaluation (IITP) grant funded by the Korea government (MSIT) (No.2022-0-00463, Development of a quantum repeater in optical fiber networks for quantum internet) (C.S., D.A.G.), the EU H2020 Research and Innovation Programme under the Marie Skłodowska-Curie grant QUDOT-TECH (861097; U.H., M.A.) and under Grant Agreement No. 871130 (Ascent+; A.R.), the EU HE EIC Pathfinder challenges action under grant agreement No. 101115575 (Q-ONE; A.R.), the Linz Institute of Technology Secure and Correct Systems Lab, supported by the State of Upper Austria (A.R.) and the FFG (Grants No. 891366 and 906046; A.R.), the Austrian Science Fund (FWF) by the research grant 10.55776/J4784 (C.S.) and via the Research Group FG5 (A.R.), the cluster of excellence

quantA [10.55776/COE1; A.R.], the German Federal Ministry of Research, Technology and Space (BMFT; grant number 16KIS2058), project MEEDGARD (J.M.K, D.E.R.). A.H. acknowledges an EPSRC DTP studentship through EP/W524311/1. B.D acknowledges an EPSRC DTP studentship through EP/D103586K/1. D.G. acknowledges the Undergraduate Research Opportunities (UROP) program at the University of Cambridge Cavendish Laboratory. D.A.G acknowledges a Royal Society University Research Fellowship. The InGaAs QD Device (Device 1) was grown in the EPSRC National Epitaxy Facility.

Appendix A: Experimental Setup

Device 1 (Device 2) is held at 4 K (3.4 K) inside a helium bath cryostat (closed-cycle cryostat) where a superconducting magnet produces a field B_z up to 8 T in the z -direction. A resonant laser and a Raman laser are combined on a beam splitter before they are sent into the cryostat. The QD emission is then coupled

back into an optical fiber before it is detected on an avalanche photodiode (APD) and time tagged with a Swabian Time Tagger. We employ cross-polarization in the photon collection path to reject the resonant readout laser, along with spectral filtering using a transmission grating setup (30 GHz full-width-at-half-maximum) to further reject the Raman laser.

The resonant laser is linearly-polarized to enable equal excitation (and collection) of both the circularly-polarized dipoles of the trion X^{1-} . We use an acousto-optical modulator (AOM) to pulse and actively stabilize the resonant laser power during experiments.

The Raman laser system consists of a pair of red-detuned lasers with equal intensities, derived from electro-optical modulation of a single narrow-linewidth laser. This is done using a fiber-coupled amplitude-electro-optical modulator (EOM) which is locked to its interferometric minimum, and is driven by microwave pulses generated from an arbitrary waveform generator (AWG). Due to a large ω_e (> 20 GHz) in Device 1 (with InGaAs QDs), we use an IQ mixer (Marki Microwave, MMIQ-0218LXPC) to upconvert the output from two channels of an AWG (Tektronix 70002B) to $\simeq 15$ GHz with a microwave signal generator (Rohde and Schwarz, SMF100) as local oscillator. In the case of Device 2 (with GaAs QDs), due to the smaller ω_e (< 5 GHz), we directly synthesize the microwave pulses in the time domain using a single channel of an AWG (Real Digital, RFSoc 4x2, up to 9.85 GSPS) instead. We build upon the *qick* firmware [59] and develop a Python library (*qeg-rfsoc* [60]) to interface with the board. We place an AOM after the EOM to pulse and actively stabilize the intensity of the Raman laser. The optics used in the Raman path is depicted in Fig. 8(a). A Swabian Pulse Streamer is used to trigger the AWG and Swabian time tagger and to generate optical pulses via electrical pulses to the AOM drivers.

Appendix B: Device Properties and Spin T_1

Device 1 consists of self-assembled InGaAs QDs embedded in a Schottky diode structure for deterministic charge control via the applied gate voltage. The heterostructure is presented in Fig. 7(a), taken from Refs. [14, 28, 43]. The gate voltage induces a d.c. Stark shift and tunes the emission wavelength of the emitter. This is depicted in the photoluminescence data presented in Fig. 7(b) where we observe the presence and the splitting of the emission lines from the neutral (X^0) and charged excitons (X^{1-} , X^{1+} and X^{2-}) at $B_z = 3.5$ T when exciting the QD with an above-band laser at 780 nm. There is a 35-nm tunnel barrier between the n-doped layer and the QDs, and a capping layer above the QD layer to prevent charge leakage. A planar cavity consisting of 20 pairs of distributed Bragg reflectors (DBR) and a super hemispherical cubic zirconia solid immersion lens are used to maximize photon

out-coupling efficiency to $\sim 10\%$ for QDs with an emission wavelength around 970 nm.

Device 2 consists of Al-droplet-etched GaAs QDs, grown via molecular beam epitaxy, in a p-i-n diode. The heterostructure is presented in Fig. 7(d). To increase the photon out-coupling, the heterostructure contains 40 pairs of DBR mirror. By applying a weak forward bias, we can deterministically charge the QD and induce a d.c. Stark shift to the emission wavelength. We observe clear splitting of the emission lines at $B_z = 6.5$ T when excited with a 632 nm above-band laser. The photoluminescence emission as a function of device bias is shown in Fig. 7(e).

We estimate the electron-spin lifetime, Γ_1^{-1} by performing time-resolved spin pumping experiments on the X^{1-} transition. By varying a delay between two resonant readout pulses, we can measure the readout counts normalized to the initialization counts as a function of delay. We extract a Γ_1^{-1} of 51(1) μ s and 43(2) μ s for Devices 1 and 2, respectively, by fitting an exponential function to the counts as a function of delay. These results are shown in Fig. 7(c) and 7(f).

Appendix C: Heavy-Hole Light-Hole Mixing and Raman Selection rules

1. Strain Hamiltonian

We follow the HH-LH mixing treatment in the presence of strain from Reference [61]. The relevant terms for understanding the spin-flipping transitions are the hole eigenstates $|J, J_z\rangle$, where $J \in \{3/2, 1/2\}$ and J_z is the projection along the growth axis. We ignore any mixing effects with the split-off band $J = 1/2$, which are negligible in comparison with mixing within the $J = 3/2$ manifold where $J_z = \pm 1/2$ and $J_z = \pm 3/2$ are the Light-Hole (LH) and Heavy-Hole (HH) states, respectively. We can then write the lowest hole eigenstates as:

$$\begin{aligned} |\uparrow\rangle &= \alpha |3/2, +3/2\rangle + \chi |3/2, +1/2\rangle + \epsilon |3/2, -1/2\rangle, \\ |\downarrow\rangle &= \alpha |3/2, -3/2\rangle - \chi^* |3/2, -1/2\rangle + \epsilon^* |3/2, +1/2\rangle, \end{aligned} \quad (\text{C1})$$

where $\alpha \lesssim 1$ parametrizes the dominant HH contribution (without loss of generality, we take α to be real and thus our phase reference), and χ and ϵ to be small complex numbers parameterizing the LH contribution. The spin flipping transitions $\uparrow \rightarrow \downarrow$ and $\downarrow \rightarrow \uparrow$ allowed by the χ term are circularly polarized and by the ϵ term π_z polarized. From the Bir-Pikus Hamiltonian, where Δ_{SO} is the spin-orbit coupling constant and e_{ij} , $i, j \in \{x, y, z\}$, is the strain tensor,

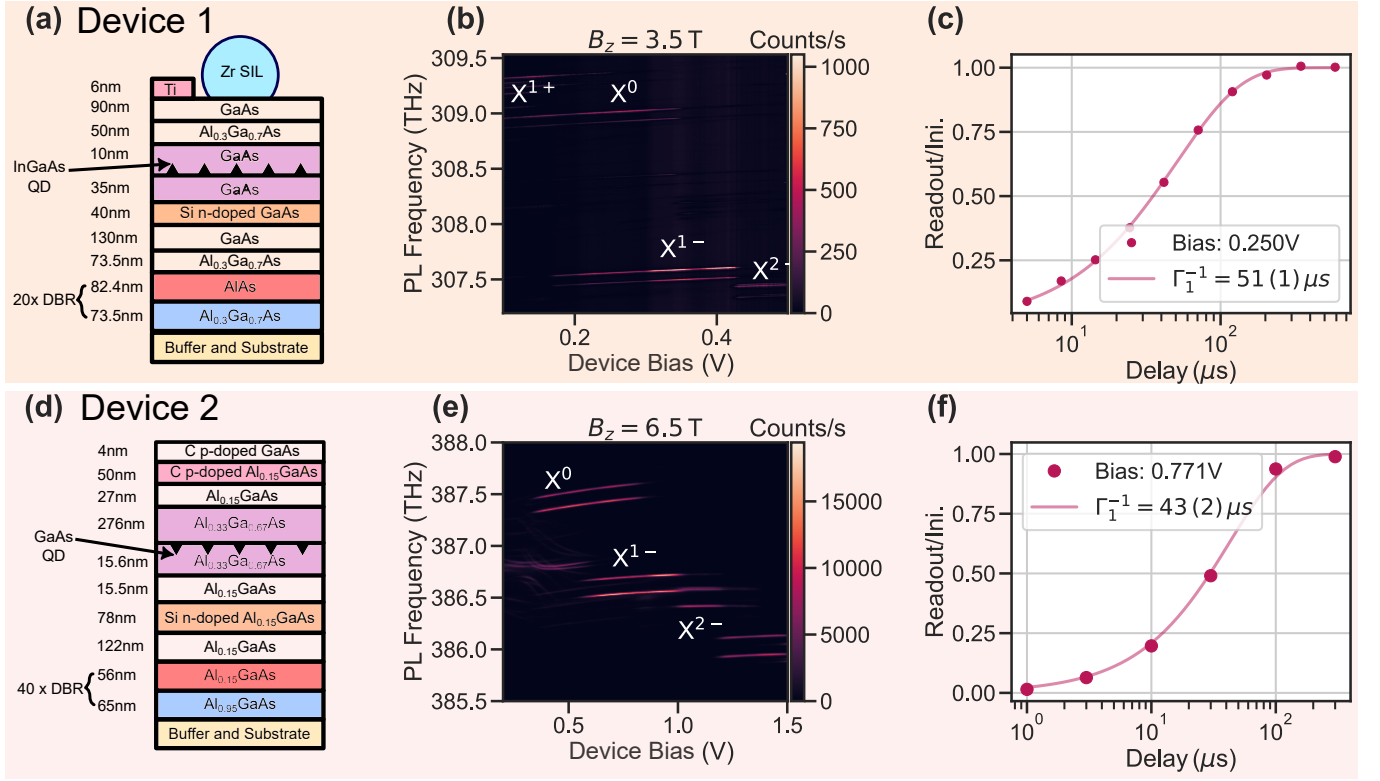


Figure 7. (a)-(c) ((d)-(f)) are measurements taken on Device 1 (Device 2). (a) and (d) are device heterostructures. (b) and (e) are photoluminescence emission frequency as a function of Device bias for above-band excitation. (c) and (f) are electron-spin relaxation experiments consisting of a resonant spin initialization (ini.) pulse, a variable delay, and a resonant spin readout pulse. The data points are the ratio of readout to initialization counts. The solid curves are fits to the data with an exponential function whose characteristic time is Γ_1^{-1} , as reported in the legend. Error bars indicate one standard error on fitted parameters.

2. Effect on Raman Transitions

For a general Raman laser polarization (where, as in our experiment, both Raman fields are the same polarization), we have two lambda systems, corresponding to two trion intermediate states, operating in parallel. The first in which the trion state with \downarrow links a spin-conserving transition in absorption, $(\Omega_{\downarrow}^{\text{sc}})^*$, and a spin-flipping transition in emission, $\Omega_{\uparrow}^{\text{sp}}$. The second in which the trion state with \uparrow links a spin-flipping transition in absorption, $(\Omega_{\downarrow}^{\text{sp}})^*$, and a spin-conserving transition in emission, $\Omega_{\uparrow}^{\text{sc}}$. The total Raman coupling between the two ground states is then:

$$\Omega = \frac{(\Omega_{\downarrow}^{\text{sc}})^* \Omega_{\uparrow}^{\text{sp}}}{2\Delta} + \frac{(\Omega_{\downarrow}^{\text{sp}})^* \Omega_{\uparrow}^{\text{sc}}}{2(\Delta + \omega_h)} \quad (\text{C3})$$

For GaAs QDs, strain contributions are small compared spin-orbit contributions, hence $\Delta_{lh} \ll \Delta_{SO}$, $|SR^*| \ll |\Delta_{SO}S^*|$ and $|S^2| \ll |R|$. As a result $\chi \approx -\sqrt{2}S^*/\Delta_{lh}$ and $\epsilon \approx R^*/\Delta_{lh}$. For InGaAs QDs, however, no strain contribution can be ignored and strain energy scales are comparable to spin-orbit coupling; as a result no simplification can be made to these terms.

between the ground states becomes:

$$\Omega = \frac{-\chi^* |\Omega_{\sigma_-}|^2}{2\Delta} + \frac{\chi^* |\Omega_{\sigma_+}|^2}{2(\Delta + \omega_h)}. \quad (\text{C4})$$

We see immediately that for $|\Omega_{\sigma_-}|^2 = |\Omega_{\sigma_+}|^2$, i.e. linearly polarized light, and in the limit where $\omega_h \ll \Delta$, the two lambda systems destructively interfere and $\Omega \rightarrow 0$, as we see for a GaAs QD (Fig. 2 and Appendix D).

If we introduce a coupling of the Raman fields to π_z – which is possible when focusing our laser through an objective with large numerical aperture taking us away from the paraxial limit – and parametrize it as a fraction η of a linearly polarized field Ω_π in-plane, then the coupling between the ground states becomes:

$$\Omega = \frac{\Omega_{\sigma_-}^* (-\chi^* \Omega_{\sigma_-} + \epsilon^* \eta \Omega_\pi)}{2\Delta} + \frac{\Omega_{\sigma_+} (\chi \Omega_{\sigma_+}^* + \epsilon^* \eta \Omega_\pi^*)}{2(\Delta + \omega_h)}. \quad (\text{C5})$$

Here a deviation from pure circular polarization would activate the π_z contribution and could enhance the Raman coupling. This would require a significant value of the ϵ LH mixing term arising for example from biaxial and in-plane shear strains. InGaAs QDs exhibit dominant biaxial strains, and this mechanism could thus explain why the optimal Raman coupling for these QDs is elliptical, as seen in Appendix G.

Appendix D: Device 2 Raman Polarization Maps Supplementary Data

The Raman fields used in our experiment consist of a pair of red-detuned lasers with equal intensities, derived from electro-optical modulation of a single narrow-linewidth laser. Fig. 8(a) shows the experimental setup of the Raman laser path where we control the polarization of the Raman laser via a pair of motorized half-wave (HWP) and quarter-wave (QWP) plates. To calibrate the angles of the HWP and the QWP, we place a polarizing beam splitter (PBS) after the two wave plates and by iteratively changing the angle of both waveplates to minimize the laser light at the reflection port of the PBS, we identify the angles that correspond to the linear horizontal polarization (i.e. (HWP, QWP) = (0, 0)).

To find the optimal optical polarization, we take the ESR spectrum, by scanning the microwave frequency applied to the electro-optical modulator and detecting the readout counts, as a function of the polarization of the Raman laser pair. We employ the following pulse sequence: nuclear-spin cooling (Rabi cooling), spin initialization with a resonant pulse, probing with a Raman drive of a fixed pulse duration of 13 ns, and spin readout with a resonant pulse. We keep the laser power fixed and the cooling and probe frequencies equal to each other, $\omega_{\text{cool}} = \omega$, for all of the scans. We first fix the angle of the HWP to 0° while iteratively varying the

angle of the QWP. We observe a variation in the readout counts, along with a shift in the resonance as we vary the QWP angle. Fig. 8(b) shows the two extreme cases, where we observe a maximal negative shift and a maximal positive shift from the bare electron splitting of $\omega_e^0 \approx 2.6$ GHz at (HWP, QWP)=(0° , 40°) and (HWP, QWP)=(0° , 110°), respectively. These polarization settings correspond to the dipoles of the two spin conserving transitions, σ_- and σ_+ , respectively, which are also identified from polarization-resolved photoluminescence measurements.

Scanning both the HWP and QWP angles while recording the readout counts confirms the dependence on the polarization of the shift in the ESR resonance. The bright regions in Fig. 8(c) and Fig. 8(d) denote the mean readout signal within the two frequency ranges where we found the ESR resonances in Fig. 8(c) (1.9-2.8 GHz and 3.5-4.5 GHz, respectively). We find a striking resemblance in the results depicted in Fig. 8(c) with the variation in the degree of circular polarization, quantified by the Stokes parameter S_3 , as a function of HWP and QWP angles, as shown in Fig. 8(e). We observe a maximum red-shifted (blue-shifted) signal in the region where $S_3 = 1$ ($S_3 = -1$), corresponding to the σ_- (σ_+) polarization. These results confirm that, for Device 2, the optimal polarization for the Raman fields is the polarization aligned to the dipole of the X^{1-} transition.

Appendix E: Intensity Noise Model and Q

To quantify the effect of laser intensity noise on the Rabi oscillation quality factor, we systematically introduce intensity modulation on the Raman laser by modulating the voltage applied to the acousto-optical modulator (AOM) used for laser intensity stabilization. We do so by combining the output of a white noise source (derived from an arbitrary waveform generator Rigol DG832) with the output of our PID controller with a power splitter before sending them to the analog modulation port of the AOM driver. This is to ensure we have a constant noise power spectral density (up to the bandwidth of the 35 MHz waveform generator) and can explore the effect of noise from low to high frequency simultaneously. A sample-and-hold protocol is implemented at the PID controller during the experiment to ensure minimal feedback from the PID controller on the external noise. By calibrating the response of the AOM on the laser power, we can convert the peak-to-peak modulation voltage to fractional (rms) intensity fluctuation dI/I . Fig. 9(a,c) and 9(b,d) show the readout counts as a function of pulse duration τ at laser noise values of dI/I of 0.00 and 0.04, respectively. Fig. 9(a, b) (c, d) are taken at $\Omega = 60$ MHz ($\Omega = 225$ MHz). The measurements are done with the same cooling Rabi frequency, $\Omega_{\text{cool}} \approx 15$ MHz as in Fig. 3. The added intensity noise clearly degrades the quality of Rabi oscillations.

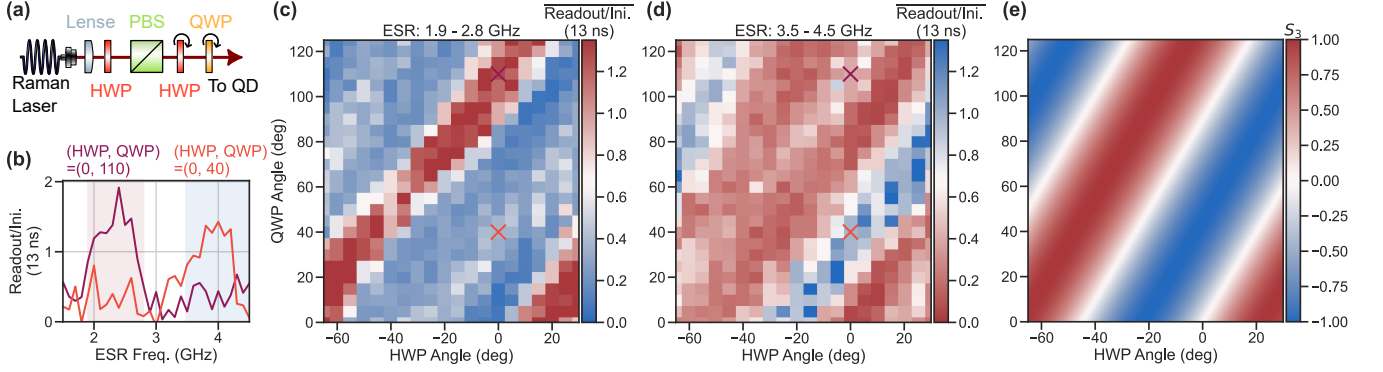


Figure 8. **Raman laser polarization control.** All measurements are taken on a GaAs QD in Device 2. (a) Schematic of the optical path for the Raman laser, highlighting the components used for polarization control. PBS: polarizing beam splitter, HWP: half-wave plate, and QWP: quarter-wave plate. (b) ESR spectrum at $(\text{HWP}, \text{QWP}) = (0, 40^\circ)$ and $(\text{HWP}, \text{QWP}) = (0, 110^\circ)$ showing a shift in the ESR resonance from the bare electron-spin splitting at $B_z = 6.5 \text{ T}$ of $\omega_e^0 \approx 2.6 \text{ GHz}$. (c) (d) Mean readout counts (normalized to the initialization counts) as a function of HWP and QWP angles in the ESR frequency range between 1.9 and 2.8 GHz (3.5 and 4.5 GHz). (e) Degree of circular polarization, quantified by the S_3 Stokes parameter as a function of HWP and QWP angles. $S_3 = 1(-1)$ yields $\sigma_- (\sigma_+)$ polarization.

To understand and fit these dynamics, we use a two-level model calculated in *Qutip* [62, 63]. We run a master equation solver, which includes collapse operators describing the decoherence mechanisms of spin relaxation Γ_1 (fixed with values taken from the result in Fig. 6(e), i.e. $\Gamma_1 = \alpha \Omega$, $\alpha = 0.0048(3)$) and spin dephasing Γ_2 (free parameter). We also include the effect of slow detuning noise (T_2^* fixed to the Ramsey measurement value of Fig. 4(b)) by repeating the master equation simulation for a set of detunings, and performing an average of the output of the simulation weighted with a normal distribution whose standard deviation σ is defined by both the laser intensity fluctuation $d\mathcal{I}/\mathcal{I}$ and the nuclear Overhauser noise σ_{OH} i.e.

$$\sigma_{laser} = d[\Delta\delta] = (\Delta\delta/\Omega) d\Omega = (\Delta\delta/\Omega) \Omega d\mathcal{I}/\mathcal{I}, \quad (\text{E1})$$

$$\sigma_{OH} = \sqrt{2}/T_2^*, \quad (\text{E2})$$

$$\sigma = \sqrt{\sigma_{laser}^2 + \sigma_{OH}^2}. \quad (\text{E3})$$

To simplify the fits over a range of $d\mathcal{I}/\mathcal{I}$ values, we first fit the measurement data (Rabi flops) at $d\mathcal{I}/\mathcal{I} = 0$ for each dataset to extract Ω (in the absence of any external laser-induced detuning noise). We find an average spin dephasing rate of $\Gamma_2/2\pi = 4.2(4) \text{ MHz}$ for all 3 measurement settings. We fix Γ_2 to this value, and for each value of Ω , we then run the simulations as a function of $d\mathcal{I}/\mathcal{I}$. The ratio of differential Stark shift to the probe Rabi frequency is fixed to the mean experimental value $\Delta\delta/\Omega = -7.4$ found in Fig. 2(f).

Solid curves in Fig. 9(a-d) are fits to our two-level model described above, allowing us to extract the Rabi quality factor from the π -pulse contrast f_π via $Q = -1/\ln(2f_\pi - 1)$, obtained from the fitted density matrix, showing a clear decrease in Q as $d\mathcal{I}/\mathcal{I}$ increases. By varying the magnitude of $d\mathcal{I}/\mathcal{I}$ in our simulation, we obtain the full set of theoretical predictions, shown

as solid curves in Fig. 9(d), for four values of Ω . These are consistent with the experimental data (also shown in Fig. 3), and thus indicate that the drop in Q at increasing $d\mathcal{I}/\mathcal{I}$ can be explained by the coupling of intensity noise to the differential Stark effect.

Appendix F: Modified Quantum Algorithmic Cooling

Figures 5(a,b) and 6(f) show the modified quantum-algorithmic cooling sequence we use to stabilize the ESR, from which we achieve an electronic $T_2^* = 74(11) \text{ ns}$. In place of the original quantum-algorithmic cooling scheme [25] (used with the InGaAs QD in Device 1), we add an extra $\pi/2$ pulse, whose phase is $\pi/2$ relative to the first $\pi/2$ pulse, following the sensing period of the algorithm and directly before the electro-nuclear interaction (hh) pulse. This additional pulse turns an electronic coherence along $\pm x$ to $\pm z$ to enable a nuclear spin flip conditioned on the electronic state with the single-sideband process allowed by the collinear hyperfine interaction (see Fig. 5(b)). The cooling algorithm uses the following parameters to obtain the data of Fig. 5(a,b) and Fig. 6(f): fixed sensing time of $t_{\text{sense}} = 55 \text{ ns}$, $N = 30$, $\Omega_{hh} \approx 47 \text{ MHz}$, $\tau_{hh} = 60 \text{ ns}$, and $\phi_{\text{sense}} = 0.875\pi$. Note that ϕ_{sense} is not $\pi/2$ here only owing to an uncompensated free precession phase. The $\pi/2$ -pulses are done at $\Omega = 125 \text{ MHz}$, corresponding to a duration of 2 ns.

Appendix G: InGaAs Supplementary Data

Fig. 10(a) shows the narrowing of the ESR resonance with Raman (top panel) and quantum-algorithmic cooling (middle panel) at $\Omega_{\text{cool}} = \Omega \approx 30 \text{ MHz}$, with a probe

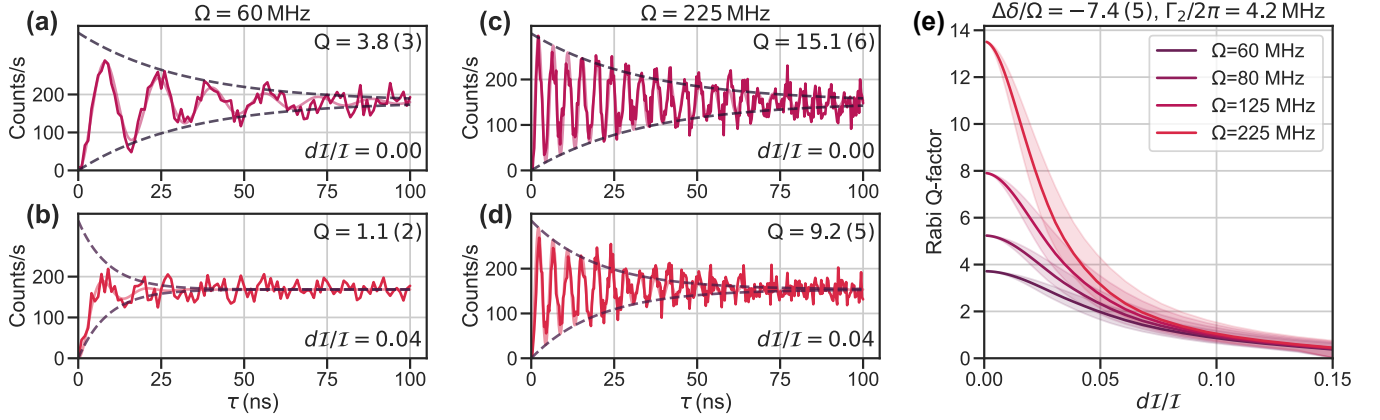


Figure 9. **Influence of laser intensity noise on the quality factor Q of Rabi oscillations.** All measurements are taken on a GaAs QD in Device 2. (a, b) Same measurement sequence as in Fig. 3. Readout counts as a function of pulse duration τ following Raman cooling ($\Omega_{\text{cool}} \approx 15$ MHz) at fractional intensity fluctuation, dI/I of 0.00 (a) and 0.04 (b) at the same probe Rabi frequency of $\Omega \approx 60$ MHz. Solid curves are fits to the data using a two-level master equation model from which we obtain Q . (c, d) Same as (a, b) but at $\Omega \approx 225$ MHz. (e) Simulated variation in Q as a function of dI/I at various probe Rabi frequencies Ω . Here, $\Delta\delta/\Omega = -7.4(5)$ and $\Gamma_2/2\pi = 4.2$ MHz. The shaded regions indicate three standard error on $\Delta\delta/\Omega$.

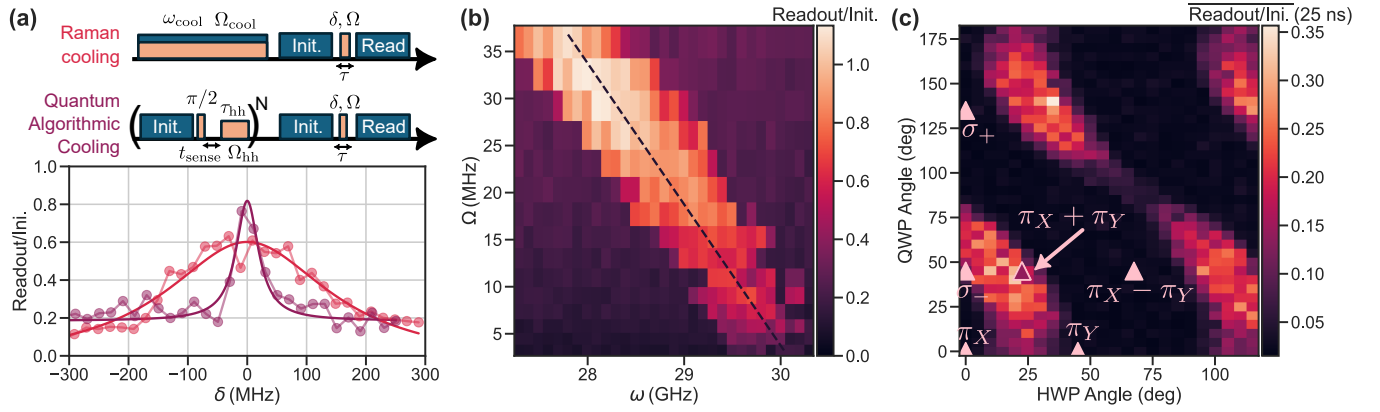


Figure 10. **Raman control and nuclear-spin cooling on an InGaAs QD in Faraday configuration.** All measurements are taken on an InGaAs QD in Device 1. (a) ESR spectroscopy. Pulse sequences (top panel) show a cooling period, with either Raman or quantum-algorithmic cooling, followed by a probe period consisting of spin initialization, ESR drive, and spin readout. The duration ratio of probe to cooling is $\approx 10\%$. The bottom panel shows the resulting data with $\Omega \sim 30$ MHz. Raman and quantum-algorithmic cooling are shown as red and purple data, respectively. A Gaussian fit (solid curves) yields linewidth (full-width-at-half-maximum) of 261(23) MHz and 53(6) MHz, respectively. At detuning δ well beyond the ESR feature, the constant value of the readout highlights the effect of spontaneous spin-flips due to optically-induced relaxation processes [27]. (b) Probe readout under Rabi cooling as a function of ESR drive frequency and Rabi frequency. The dashed line highlights a linear negative shift in the ESR resonance from the bare electron splitting of $\omega_e^0 \approx 30$ GHz. (c) Maximum readout counts in an ESR spectrum at a fixed Raman laser power (corresponding to $\Omega \sim 20$ MHz), under Rabi cooling, as a function of the polarization of the Raman laser, as controlled by rotating half-wave-plate (HWP) and quarter-wave-plate (QWP) angles (referenced to the linearly horizontal polarization π_X). Polarizations of interest are highlighted with triangles.

pulse duration set to the π -pulse time of $\tau = 17$ ns. For quantum-algorithmic cooling, we optimize the cooling parameters to be $\tau_{hh} = 105$ ns, t_{sense} chirped from 10 ns to 200 ns in $N = 30$ steps. We achieve an ESR linewidth (at full-width-at-half-maximum) of 261(23) MHz and 53(6) MHz for Raman and quantum-algorithmic cooling, respectively.

We also observe the effect of the differential Stark shift

on the ESR resonance, shown in Fig. 10(b). We take ESR spectra as a function of Ω , and observe a negative shift in the ESR resonance as a function of Ω . These data yield $\Delta\delta/\Omega = -65(2)$ from a linear fit, and a corresponding Rabi frequency imbalance of $\eta = 129(5)$. We can then vary the polarization of the Raman laser pair to optimize the readout signal integrated over the ESR frequency range 25-35 GHz (i.e. ± 5 GHz around the bare ESR res-

onance of $\omega_e^0 = 30$ GHz), as shown in Fig. 10(c). In contrast to our measurement on a GaAs QD (Fig. 2) where we found maximum readout signal with pure circular polarization, we find here that a degree of diagonal polarization $\pi_X + \pi_Y$ results in the highest readout signal. This polarization setting is used for the electron-spin control measurements shown in Fig. 10(a-b) and Fig. 6(a-c).

Appendix H: Three-level Model for CPT

We start with the Hamiltonian of a three-level system,

$$\begin{aligned} \mathcal{H}_{3LS} = & \hbar\Delta |e\rangle \langle e| + \hbar\delta |\uparrow\rangle \langle \uparrow| \\ & + \hbar\Omega_{\downarrow}/2 (|\downarrow\rangle \langle e| + |e\rangle \langle \downarrow|) \\ & + \hbar\Omega_{\uparrow}/2 (|\uparrow\rangle \langle e| + |e\rangle \langle \uparrow|), \end{aligned}$$

where $|\downarrow\rangle$ and $|\uparrow\rangle$ are the two electron-spin ground states linked by a trion excited state $|e\rangle \equiv |\downarrow\downarrow\uparrow\rangle$, $\delta = \omega - \omega_e^0$ is the detuning from two-photon resonance, and Δ is the single-photon detuning. The resonant Rabi frequencies for each transition from the excited state are labeled as Ω_{\downarrow} or Ω_{\uparrow} . We include the collapse operators that define the ground-state relaxation Γ_1 and dephasing rate Γ_2 , along with the spontaneous relaxation from the excited state along the spin-conserving $\gamma_{SC} \approx \gamma_1$ and spin-flipping γ_{SP} channels as $\hat{C}_1 = \sqrt{\Gamma_1/2} (|\downarrow\rangle \langle \uparrow| + |\uparrow\rangle \langle \downarrow|)$, $\hat{C}_2 = \sqrt{\Gamma_2/2} (|\downarrow\rangle \langle \downarrow| - |\uparrow\rangle \langle \uparrow|)$, $\hat{C}_3 = \sqrt{\gamma_1} |\downarrow\rangle \langle e|$ and $\hat{C}_4 = \sqrt{\gamma_{SP}} |\uparrow\rangle \langle e|$, respectively.

To fit the data, we fix $\Delta = 0$ and the ground and excited state relaxation rates to be $\Gamma_1^{-1} = 45000$ ns, $\gamma_1^{-1} = 0.25$ ns and $\gamma_{SP}^{-1} = 100$ ns. We then keep ω_e^0 , Ω_{\uparrow} , Ω_{\downarrow} and Γ_2 as free fitting parameters, and ω as our control axis. By fitting to the data in Fig. 2(b), we obtain $\omega_e^0/2\pi = 2.60(1)$ GHz, $\Omega_{\downarrow} = 9.3(3)$ ns $^{-1}$, $\Omega_{\uparrow} = 0.19(2)$ ns $^{-1}$ and $\Gamma_2 = 0.53(8)$ ns $^{-1}$. Given that the saturation Rabi frequency $\Omega_{\text{sat}} = \gamma_1/\sqrt{2} = 2.82$ ns $^{-1}$, we can represent both Rabi frequencies in terms of Ω_{sat} , such that $\Omega_{\downarrow} = 3.29(9) \Omega_{\text{sat}}$ and $\Omega_{\uparrow} = 0.069(8) \Omega_{\text{sat}}$. The former is consistent with the pump power used in the experiment ($\approx 10 P_{\text{sat}}$, hence $\Omega_{\downarrow} \approx \sqrt{10} \Omega_{\text{sat}}$).

Appendix I: Four-level Model for Raman-driven Rabi Oscillations

We consider a four-level system consisting of two spin states $|\uparrow\rangle$ and $|\downarrow\rangle$ in the ground state manifold, where a single electron occupies the QD. In the excited state manifold we account for two X^{1-} states $|\uparrow\downarrow\uparrow\rangle$ and $|\downarrow\downarrow\uparrow\rangle$. A sketch of the system is shown in Fig. 11.

In Faraday geometry, the Hamiltonian of the system can be separated into the system Hamiltonian H_0 and the part accounting for the light-matter interaction H_{int}

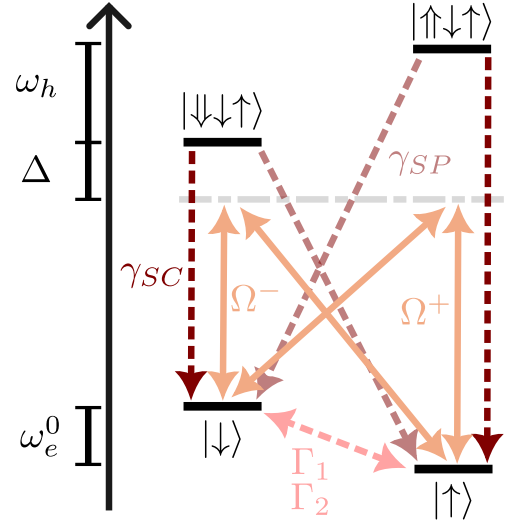


Figure 11. Four-level system. Solid arrows represent detuned Raman drive. Dashed arrows represent Lindblad operators, where we include the trion relaxation rates (γ_{SC} and γ_{SP}), along with the ground state electron relaxation (Γ_1) and dephasing (Γ_2) rates.

via

$$H = H_0 + H_{\text{int}}. \quad (I1)$$

Setting the energies of the states, such that $E_{|\downarrow\rangle} = 0$, $E_{|\uparrow\rangle} = -\hbar\omega_e^0$ and $E_{|\uparrow\downarrow\uparrow\rangle} = E_{\text{trion}}$ and $E_{|\downarrow\downarrow\uparrow\rangle} = E_{\text{trion}} + \hbar\omega_h$, where the magnetic field has induced a Zeeman splitting of electrons (ω_e^0) and holes (ω_h). We write the Hamiltonian in a rotating frame set to the laser pulse between $|\downarrow\rangle$ and $|\downarrow\downarrow\uparrow\rangle$, resulting in the detuning Δ , such that

$$\begin{aligned} H_0 = & 0 |\downarrow\rangle \langle \downarrow| - \hbar\omega_e |\uparrow\rangle \langle \uparrow| \\ & + \Delta |\downarrow\downarrow\uparrow\rangle \langle \downarrow\downarrow\uparrow| + (\Delta + \hbar\omega_h) |\uparrow\downarrow\uparrow\rangle \langle \uparrow\downarrow\uparrow| \end{aligned} \quad (I2)$$

The light-matter interaction in standard rotating wave and dipole approximation reads

$$\begin{aligned} H_{\text{int}} = & -\hbar (\Omega^- |\downarrow\downarrow\uparrow\rangle \langle \downarrow| - \Omega^+ |\uparrow\downarrow\uparrow\rangle \langle \uparrow|) \\ & - \hbar \frac{1}{\sqrt{\mathcal{C}}} (\Omega^- |\downarrow\downarrow\uparrow\rangle \langle \uparrow| - \Omega^+ |\uparrow\downarrow\uparrow\rangle \langle \downarrow|) + h.c. \end{aligned} \quad (I3)$$

The cyclicity \mathcal{C} is used to tune the ratio between strong spin-conserving and weak spin-flipping transitions. The choice of rotating frame at Ω_1 acting between $|\downarrow\rangle$ and $|\uparrow\downarrow\uparrow\rangle$ results in the laser pulse Ω_2 acting between $|\uparrow\rangle$ and $|\downarrow\downarrow\uparrow\rangle$ to be detuned by Δ_{RF} with respect to the rotating frame. The left (Ω^-) and right (Ω^+) circularly polarized components of the envelope are given by

$$\Omega^- = \frac{1+i}{2} (\Omega_1 + \Omega_2 \exp^{-i\Delta_{\text{RF}}t}) \quad (I4)$$

$$\Omega^+ = \frac{1-i}{2} (\Omega_1 + \Omega_2 \exp^{-i\Delta_{\text{RF}}t}). \quad (I5)$$

To describe relaxation processes from the trions to the ground states, we use Lindblad rates $\Gamma'_i \in \{\gamma_{SC}, \gamma_{SP}\}$ and their corresponding Lindblad operators L_i . We also employ a Lindblad term to account for a direct relaxation between both ground states at rate Γ_1 . Furthermore, we take into account the dephasing of electron ground state coherences by exponentially damping them with a constant damping rate Γ_2 . These processes are shown in Fig. 11 by dashed arrows.

This leads to the equations of motions for a density matrix

$$\dot{\rho} = -\frac{i}{\hbar} [H, \rho] + \sum_i \Gamma'_i \left(L_i \rho L_i^\dagger - \frac{1}{2} \{ L_i^\dagger L_i, \rho \} \right). \quad (I6)$$

We solve this equation numerically to calculate the dynamics of the system. To include the effect of the finite dephasing, evident from the decay time scale (T_2^* value)

and the order ($n=2$) from the free-induction decay experiments, we perform a weighted average on $\rho(t, \omega)$, i.e.

$$\rho_{\text{ensemble}}(t) = \int w(\omega) \rho(t, \omega) d\omega \quad (I7)$$

with the weight function modeled as a Gaussian noise with $\sigma = \sqrt{2}/T_2^*$,

$$w(\omega) = \frac{1}{\sigma\sqrt{2\pi}} \exp^{-\frac{1}{2} \left(\frac{\omega - \omega_e}{\sigma} \right)^2} \quad (I8)$$

is performed. The output of the ensemble average results in the fits shown in Fig. 3 and 6, where we have also set $\Omega^+ = 0$ to match the experimental configuration.

-
- [1] H. J. Kimble, The quantum internet, *Nature* **453**, 1023–1030 (2008).
- [2] S. Ritter, C. Nölleke, C. Hahn, A. Reiserer, A. Neuzner, M. Uphoff, M. Mücke, E. Figueroa, J. Bochmann, and G. Rempe, An elementary quantum network of single atoms in optical cavities, *Nature* **484**, 195–200 (2012).
- [3] M. Ruf, N. H. Wan, H. Choi, D. Englund, and R. Hanson, Quantum networks based on color centers in diamond, *Journal of Applied Physics* **130**, 070901 (2021).
- [4] L.-M. Duan, M. D. Lukin, J. I. Cirac, and P. Zoller, Long-distance quantum communication with atomic ensembles and linear optics, *Nature* **414**, 413–418 (2001).
- [5] N. Sangouard, C. Simon, H. de Riedmatten, and N. Gisin, Quantum repeaters based on atomic ensembles and linear optics, *Rev. Mod. Phys.* **83**, 33 (2011).
- [6] A. Gritsch, A. Ulanowski, J. Pforr, and A. Reiserer, Optical single-shot readout of spin qubits in silicon, *Nature Communications* **16**, 64 (2025).
- [7] M. Raha, S. Chen, C. M. Phenicie, S. Ourari, A. M. Dibos, and J. D. Thompson, Optical quantum nondemolition measurement of a single rare earth ion qubit, *Nature Communications* **11**, 1605 (2020).
- [8] P.-J. Stas, Y. Q. Huan, B. Machielse, E. N. Knall, A. Suleymanzade, B. Pingault, M. Sutula, S. W. Ding, C. M. Knaut, D. R. Assumpcao, Y.-C. Wei, M. K. Bhaskar, R. Riedinger, D. D. Sukachev, H. Park, M. Lončar, D. S. Levonian, and M. D. Lukin, Robust multi-qubit quantum network node with integrated error detection, *Science* **378**, 557 (2022).
- [9] X. Guo, A. M. Stramma, Z. Li, W. G. Roth, B. Huang, Y. Jin, R. A. Parker, J. A. Martínez, N. Shofer, C. P. Michaels, C. P. Purser, M. H. Appel, E. M. Alexeev, T. Liu, A. C. Ferrari, D. D. Awschalom, N. Deegan, B. Pingault, G. Galli, F. J. Heremans, M. Atatüre, and A. A. High, Microwave-based quantum control and coherence protection of tin-vacancy spin qubits in a strain-tuned diamond-membrane heterostructure, *Physical Review X* **13**, 041037 (2023).
- [10] P. Senellart, G. Solomon, and A. White, High-performance semiconductor quantum-dot single-photon sources, *Nature Nanotechnology* **12**, 1026 (2017).
- [11] L. Zhai, G. N. Nguyen, C. Spinnler, J. Ritzmann, M. C. Löbl, A. D. Wieck, A. Ludwig, A. Javadi, and R. J. Warburton, Quantum interference of identical photons from remote GaAs quantum dots, *Nature Nanotechnology* **17**, 829–833 (2022).
- [12] N. Tomm, A. Javadi, N. O. Antoniadis, D. Najer, M. C. Löbl, A. R. Korsch, R. Schott, S. R. Valentin, A. D. Wieck, A. Ludwig, and R. J. Warburton, A bright and fast source of coherent single photons, *Nature Nanotechnology* **16**, 399–403 (2021).
- [13] M. H. Appel, A. Tiranov, A. Javadi, M. C. Löbl, Y. Wang, S. Scholz, A. D. Wieck, A. Ludwig, R. J. Warburton, and P. Lodahl, Coherent spin-photon interface with waveguide induced cycling transitions, *Phys. Rev. Lett.* **126**, 013602 (2021).
- [14] D. A. Gangloff, G. Éthier Majcher, C. Lang, E. V. Denning, J. H. Bodey, D. M. Jackson, E. Clarke, M. Hugues, C. Le Gall, and M. Atatüre, Quantum interface of an electron and a nuclear ensemble, *Science* **364**, 62–66 (2019).
- [15] E. A. Chekhovich, S. F. C. da Silva, and A. Rastelli, Nuclear spin quantum register in an optically active semiconductor quantum dot, *Nature Nanotechnology* **15**, 999–1004 (2020).
- [16] N. Shofer, L. Zaporski, M. Hayhurst Appel, S. Manna, S. Covre da Silva, A. Ghorbal, U. Haeusler, A. Rastelli, C. Le Gall, M. Gawelczyk, M. Atatüre, and D. A. Gangloff, Tuning the coherent interaction of an electron qubit and a nuclear magnon, *Phys. Rev. X* **15**, 021004 (2025).
- [17] M. H. Appel, A. Ghorbal, N. Shofer, L. Zaporski, S. Manna, S. F. C. da Silva, U. Haeusler, C. Le Gall, A. Rastelli, D. A. Gangloff, and M. Atatüre, A many-body quantum register for a spin qubit, *Nature Physics* **21**, 368–373 (2025).
- [18] L. Zaporski, N. Shofer, J. H. Bodey, S. Manna, G. Gillard, M. H. Appel, C. Schimpf, S. F. Covre da Silva, J. Jarman, G. Delamare, G. Park, U. Haeusler, E. A. Chekhovich, A. Rastelli, D. A. Gangloff, M. Atatüre, and C. Le Gall, Ideal refocusing of an optically active spin qubit under strong hyperfine interactions, *Nature Nanotechnology* **18**, 257–263 (2023).
- [19] H. E. Dyte, S. Manna, S. F. C. da Silva, A. Rastelli, and

- E. A. Chekhovich, Storing quantum coherence in a quantum dot nuclear spin ensemble for over 100 milliseconds, [arXiv:2502.11092](https://arxiv.org/abs/2502.11092) (2025).
- [20] H. Huet, P. R. Ramesh, S. C. Wein, N. Coste, P. Hilaire, N. Somaschi, M. Morassi, A. Lemaître, I. Sagnes, M. F. Doty, O. Krebs, L. Lanco, D. A. Fioretto, and P. Senellart, Deterministic and reconfigurable graph state generation with a single solid-state quantum emitter, *Nature Communications* **16**, 4337 (2025).
- [21] A. Nick Vamivakas, Y. Zhao, C.-Y. Lu, and M. Atatüre, Spin-resolved quantum-dot resonance fluorescence, *Nature Physics* **5**, 198 (2009).
- [22] A. Delteil, W.-b. Gao, P. Fallahi, J. Miguel-Sanchez, and A. Imamoglu, Observation of quantum jumps of a single quantum dot spin using submicrosecond single-shot optical readout, *Phys. Rev. Lett.* **112**, 116802 (2014).
- [23] A. N. Vamivakas, C.-Y. Lu, C. Matthiesen, Y. Zhao, S. Fält, A. Badolato, and M. Atatüre, Observation of spin-dependent quantum jumps via quantum dot resonance fluorescence, *Nature* **467**, 297 (2010).
- [24] N. O. Antoniadis, M. R. Hogg, W. F. Stehl, A. Javadi, N. Tomm, R. Schott, S. R. Valentin, A. D. Wieck, A. Ludwig, and R. J. Warburton, Cavity-enhanced single-shot readout of a quantum dot spin within 3 nanoseconds, *Nature Communications* **14**, 3977 (2023).
- [25] D. M. Jackson, U. Haeusler, L. Zaporoski, J. H. Bodey, N. Shofer, E. Clarke, M. Hugues, M. Atatüre, C. Le Gall, and D. A. Gangloff, Optimal purification of a spin ensemble by quantum-algorithmic feedback, *Phys. Rev. X* **12**, 031014 (2022).
- [26] D. Press, T. D. Ladd, B. Zhang, and Y. Yamamoto, Complete quantum control of a single quantum dot spin using ultrafast optical pulses, *Nature* **456**, 218 (2008).
- [27] J. H. Bodey, R. Stockill, E. V. Denning, D. A. Gangloff, G. Éthier Majcher, D. M. Jackson, E. Clarke, M. Hugues, C. L. Gall, and M. Atatüre, Optical spin locking of a solid-state qubit, *npj Quantum Information* **5**, 95 (2019).
- [28] D. M. Jackson, D. A. Gangloff, J. H. Bodey, L. Zaporoski, C. Bachorz, E. Clarke, M. Hugues, C. Le Gall, and M. Atatüre, Quantum sensing of a coherent single spin excitation in a nuclear ensemble, *Nature Physics* **17**, 585–590 (2021).
- [29] M. R. Hogg, N. O. Antoniadis, M. A. Marczak, G. N. Nguyen, T. L. Baltisberger, A. Javadi, R. Schott, S. R. Valentin, A. D. Wieck, A. Ludwig, and R. J. Warburton, Fast optical control of a coherent hole spin in a microcavity, *Nature Physics* **21**, 1475–1481 (2025).
- [30] T. M. Sweeney, S. G. Carter, A. S. Bracker, M. Kim, C. S. Kim, L. Yang, P. M. Vora, P. G. Brereton, E. R. Cleveland, and D. Gammon, Cavity-stimulated raman emission from a single quantum dot spin, *Nature Photonics* **8**, 442–447 (2014).
- [31] C. Schimpf, A. J. Garcia, Z. X. Koong, G. N. Nguyen, L. L. Niekamp, M. H. Appel, A. Hassanen, J. Waller, Y. Karli, S. P. C. da Silva, J. Ritzmann, H.-G. Babin, A. D. Wieck, A. Pishchagin, N. Margaria, T.-H. Au, S. Bossier, M. Morassi, A. Lemaître, P. Senellart, N. Somaschi, A. Ludwig, R. Warburton, M. Atatüre, A. Rastelli, M. Gawelczyk, and D. Gangloff, Optical and magnetic response by design in gaas quantum dots, *PRX Quantum*, (2025).
- [32] N. H. Lindner and T. Rudolph, Proposal for Pulsed On-Demand Sources of Photonic Cluster State Strings, *Physical Review Letters* **103**, 113602 (2009).
- [33] C. P. Michaels, J. Arjona Martínez, R. Debroux, R. A. Parker, A. M. Stramma, L. I. Huber, C. M. Purser, M. Atatüre, and D. A. Gangloff, Multidimensional cluster states using a single spin-photon interface coupled strongly to an intrinsic nuclear register, *Quantum* **5**, 565 (2021).
- [34] M. Bayer, G. Ortner, O. Stern, A. Kuther, A. A. Gorbunov, A. Forchel, P. Hawrylak, S. Fafard, K. Hinzer, T. L. Reinecke, S. N. Walck, J. P. Reithmaier, F. Klopff, and F. Schäfer, Fine structure of neutral and charged excitons in self-assembled in(ga)as/(al)gaas quantum dots, *Phys. Rev. B* **65**, 195315 (2002).
- [35] A. V. Koudinov, I. A. Akimov, Y. G. Kusrayev, and F. Henneberger, Optical and magnetic anisotropies of the hole states in stranski-krastanov quantum dots, *Phys. Rev. B* **70**, 241305 (2004).
- [36] T. Belhadj, T. Amand, A. Kunold, C.-M. Simon, T. Kuroda, M. Abbarchi, T. Mano, K. Sakoda, S. Kunz, X. Marie, and B. Urbaszek, Impact of heavy hole-light hole coupling on optical selection rules in gaas quantum dots, *Applied Physics Letters* **97**, 051111 (2010).
- [37] Y. H. Huo, B. J. Witek, S. Kumar, J. R. Cardenas, J. X. Zhang, N. Akopian, R. Singh, E. Zallo, R. Grifone, D. Krieger, R. Trotta, F. Ding, J. Stangl, V. Zwiller, G. Bester, A. Rastelli, and O. G. Schmidt, A light-hole exciton in a quantum dot, *Nature Physics* **10**, 46–51 (2013).
- [38] B. Urbaszek, X. Marie, T. Amand, O. Krebs, P. Voisin, P. Maletinsky, A. Högele, and A. Imamoglu, Nuclear spin physics in quantum dots: An optical investigation, *Reviews of Modern Physics* **85**, 79 (2013).
- [39] D. N. Krizhanovskii, A. Ebbens, A. I. Tartakovskii, F. Pulizzi, T. Wright, M. S. Skolnick, and M. Hopkinson, Individual neutral and charged $\text{In}_x\text{Ga}_{1-x}\text{As}$ -GaAs quantum dots with strong in-plane optical anisotropy, *Phys. Rev. B* **72**, 161312 (2005).
- [40] Y. H. Huo, V. Krápek, O. G. Schmidt, and A. Rastelli, Spontaneous brightening of dark excitons in gaas/algaas quantum dots near a cleaved facet, *Physical Review B* **95**, 165304 (2017).
- [41] A. V. Kuhlmann, J. Houel, D. Brunner, A. Ludwig, D. Reuter, A. D. Wieck, and R. J. Warburton, A dark-field microscope for background-free detection of resonance fluorescence from single semiconductor quantum dots operating in a set-and-forget mode, *Review of Scientific Instruments* **84**, 073905 (2013).
- [42] C.-Y. Lu, Y. Zhao, A. N. Vamivakas, C. Matthiesen, S. Fält, A. Badolato, and M. Atatüre, Direct measurement of spin dynamics in inas/gaas quantum dots using time-resolved resonance fluorescence, *Physical Review B* **81**, 035332 (2010).
- [43] R. Stockill, M. J. Stanley, L. Huthmacher, E. Clarke, M. Hugues, A. J. Miller, C. Matthiesen, C. Le Gall, and M. Atatüre, Phase-Tuned Entangled State Generation between Distant Spin Qubits, *Physical Review Letters* **119**, 010503 (2017).
- [44] L. Zhai, M. C. Löbl, G. N. Nguyen, J. Ritzmann, A. Javadi, C. Spinnler, A. D. Wieck, A. Ludwig, and R. J. Warburton, Low-noise gaas quantum dots for quantum photonics, *Nature Communications* **11**, 4745 (2020).
- [45] J. Dreiser, M. Atatüre, C. Galland, T. Müller, A. Badolato, and A. Imamoglu, Optical investigations of quantum dot spin dynamics as a function of external electric and magnetic fields, *Physical Review B* **77**, 075317 (2008).

- [46] E. I. Rosenthal, S. Biswas, G. Scuri, H. Lee, A. J. Stein, H. C. Kleidermacher, J. Grzesik, A. E. Rugar, S. Aghaeimeibodi, D. Riedel, M. Titze, E. S. Bielejec, J. Choi, C. P. Anderson, and J. Vučković, Single-shot readout and weak measurement of a tin-vacancy qubit in diamond, *Physical Review X* **14**, 041008 (2024).
- [47] G. N. Nguyen, C. Spinnler, M. R. Hogg, L. Zhai, A. Javadi, C. A. Schrader, M. Erbe, M. Wyss, J. Ritzmann, H.-G. Babin, A. D. Wieck, A. Ludwig, and R. J. Warburton, Enhanced electron-spin coherence in a GaAs quantum emitter, *Phys. Rev. Lett.* **131**, 210805 (2023).
- [48] X. Xu, B. Sun, P. R. Berman, D. G. Steel, A. S. Bracker, D. Gammon, and L. J. Sham, Coherent population trapping of an electron spin in a single negatively charged quantum dot, *Nature Physics* **4**, 692–695 (2008).
- [49] D. Brunner, B. D. Gerardot, P. A. Dalgarno, G. Wüst, K. Karrai, N. G. Stoltz, P. M. Petroff, and R. J. Warburton, A coherent single-hole spin in a semiconductor, *Science* **325**, 70–72 (2009).
- [50] G. Éthier-Majcher, D. Gangloff, R. Stockill, E. Clarke, M. Hugues, C. Le Gall, and M. Atatüre, Improving a solid-state qubit through an engineered mesoscopic environment, *Physical Review Letters* **119**, 130503 (2017).
- [51] A. Bechtold, D. Rauch, F. Li, T. Simmet, P.-L. Ardelit, A. Regler, K. Müller, N. A. Sinitsyn, and J. J. Finley, Three-stage decoherence dynamics of an electron spin qubit in an optically active quantum dot, *Nature Physics* **11**, 1005 (2015).
- [52] R. Stockill, C. L. Gall, C. Matthiesen, L. Huthmacher, E. Clarke, M. Hugues, and M. Atatüre, Quantum dot spin coherence governed by a strained nuclear environment, *Nature Communications* **7**, 12745 (2016).
- [53] T. Botzem, R. P. G. McNeil, J.-M. Mol, D. Schuh, D. Bougeard, and H. Bluhm, Quadrupolar and anisotropy effects on dephasing in two-electron spin qubits in GaAs, *Nature Communications* **7**, 11170 (2016).
- [54] A. Högele, M. Kroner, C. Latta, M. Claassen, I. Carusotto, C. Bulutay, and A. Imamoglu, Dynamic nuclear spin polarization in the resonant laser excitation of an InGaAs quantum dot, *Physical Review Letters* **108**, 197403 (2012).
- [55] D. Farfurnik, H. Singh, Z. Luo, A. S. Bracker, S. G. Carter, R. M. Pettit, and E. Waks, All-optical noise spectroscopy of a solid-state spin, *Nano Letters* **23**, 1781 (2023).
- [56] E. A. Chekhovich, I. M. Griffiths, M. S. Skolnick, H. Huang, S. F. C. da Silva, X. Yuan, and A. Rastelli, Cross calibration of deformation potentials and gradient-elastic tensors of GaAs using photoluminescence and nuclear magnetic resonance spectroscopy in GaAs/AlGaAs quantum dot structures, *Physical Review B* **97**, 235311 (2018).
- [57] X. Ding, Y. He, Z.-C. Duan, N. Gregersen, M.-C. Chen, S. Unsleber, S. Maier, C. Schneider, M. Kamp, S. Höfling, C.-Y. Lu, and J.-W. Pan, On-Demand Single Photons with High Extraction Efficiency and Near-Unity Indistinguishability from a Resonantly Driven Quantum Dot in a Micropillar, *Physical Review Letters* **116**, 020401 (2016).
- [58] R. Uppu, F. T. Pedersen, Y. Wang, C. T. Olesen, C. Papon, X. Zhou, L. Midolo, S. Scholz, A. D. Wieck, A. Ludwig, and P. Lodahl, Scalable integrated single-photon source, *Science Advances* **6**, abc8268 (2020).
- [59] L. Stefanazzi, K. Treptow, N. Wilcer, C. Stoughton, C. Bradford, S. Uemura, S. Zorzetti, S. Montella, G. Cancelo, S. Sussman, A. Houck, S. Saxena, H. Arnaldi, A. Agrawal, H. Zhang, C. Ding, and D. I. Schuster, The QICK (Quantum Instrumentation Control Kit): Readout and control for qubits and detectors, *Review of Scientific Instruments* , 044709 (2022).
- [60] D. J. Graham and Z. X. Koong, [danieljamesgraham/qeg-rfsoc: Initial doi release](https://arxiv.org/abs/2501.04470) (2025).
- [61] J. Wang, G. C. Guo, and L. He, Theory of strain tuning fine structure splitting in self-assembled InGaAs quantum dots, *Journal of Physics: Condensed Matter* **26**, 475301 (2014).
- [62] J. Johansson, P. Nation, and F. Nori, QuTiP: An open-source Python framework for the dynamics of open quantum systems, *Computer Physics Communications* **183**, 1760 (2012).
- [63] J. Johansson, P. Nation, and F. Nori, QuTiP 2: A Python framework for the dynamics of open quantum systems, *Computer Physics Communications* **184**, 1234 (2013).